12-2009

Laboratory Generation and Physics of Propagation of Solitary Waves and Water Surface Depressions

Siamak Malek mohammadi
Clemson University, smalekm@gmail.com

LABORATORY GENERATION AND PHYSICS OF PROPAGATION OF SOLITARY WAVES AND WATER SURFACE DEPRESSIONS

A Dissertation
Presented to
the Graduate School of
Clemson University

In Partial Fulfillment
of the Requirements for the Degree
Doctor of Philosophy
Civil Engineering

---

by
Siamak Malek Mohammadi
December 2009

Accepted by:
Dr. Firat Y. Testik, Committee Chair
Dr. Nadim Aziz
Dr. Abdul A. Khan
Dr. Earl J. Hayter

ABSTRACT

Solitary waves and water surface depressions are generated using a piston-type wavemaker. Different aspects of their propagation including profile evolution, establishment rate, stability, and celerity are examined experimentally.

Traditionally, solitary waves are generated in laboratory set-ups using a methodology developed by Goring (1979) that considers a wave of permanent form during the generation process. A New methodology for generation of solitary waves using piston-type wavemakers is proposed by considering the evolving nature of the wave during generation phase. The capability of the New methodology in generation of solitary waves is assessed by conducting a series of laboratory experiments in water depth, h, of 20 *cm* and for the dimensionless wave height, H/h, values (H – wave height) ranging from 0.3 to 0.6. Waves generated using the Goring methodology served as a benchmark to evaluate the performance of the New methodology in generating solitary waves. Recorded waveforms are compared with theoretical solutions in terms of various wave characteristics (e.g., wave height, profile shape, wave celerity). These comparisons revealed that the New methodology is capable of generating more accurate and rapidly-established solitary waves with less wave attenuation with distance compared to the Goring methodology.

In the second part, water surface depressions are generated using the Goring methodology in water depths of 6, 10 and 30 *cm* and for the dimensionless trough amplitude, a_t/h, values (a_t – trough amplitude) ranging from 0.05 to 0.6. Generated water

surface depressions are in good agreement with the aimed theoretical profile in the vicinity of the wave paddle. In all experiments, generated negative solitary wave-like depression wave rapidly deforms into a triangular-like depression wave followed by a series of oscillatory trailing waves. As the depression wave propagates, as a result of nonlinear and dispersive effects its amplitude attenuates, slope of the leading edge of the depression wave becomes gentler while its rear edge slope becomes steeper. The amplitudes of the oscillatory trailing waves increase initially as the depression propagates; then the amplitudes of the oscillatory trailing waves start attenuating with distance due to viscous and dispersive effects. Celerity of the depression wave increases with distance as the depression amplitude attenuates with distance, but it never reaches the celerity of long waves in deep waters. Based on the experimental data of the present study and those reported by Hammack and Segur (1978), three empirical equations are proposed to predict the profile shape of a depression (i.e. trough amplitude, frequency of the leading half, and slope of the rear edge) for a given propagation distance.

DEDICATION

This thesis is dedicated to my parents, whose never-ending love, support, and sacrifices have made this possible. They have waited so long for this moment to come true; I am glad that their waiting has finally been rewarded. This work is also dedicated to my sisters whose love and support have backed me up to keep moving on.

ACKNOWLEDGMENTS

Dr. Firat Y. Testik, my thesis advisor, generously provided guidance, encouragement and assistance in all aspects of the project. I would like to extend my appreciation to examining committee members, Dr. Nadim Aziz, Dr. Abdul Khan, and Dr. Earl Hayter for their constructive comments, which enhanced my knowledge of the physical processes and also improved the quality of the present manuscript.

This research was supported by the funds provided by College of Engineering and Science at Clemson University.

TABLE OF CONTENTS

Page

LIST OF TABLES

LIST OF FIGURES

List of Figures (Continued)

CHAPTER ONE

INTRODUCTION

Tsunamis are very long waves that are mainly generated due to underwater geophysical dislocations such as submarine earthquakes, landslides, volcanic eruptions and underwater explosions. These waves propagate across the ocean with very high speeds. As they reach the continental shelf and approach the shoreline, they decelerate and this deceleration results in piling-up of water and may lead to very large wave heights at the shoreline. . Tsunamis are frequently referred to as "Killer Waves" since when they attack the populated coastal areas worldwide they cause tremendous damages of coastal infrastructures, noteworthy amounts of loss of lives, and a variety of additional long-term social and health-related issues. The deadliest and most recent tsunami was generated by the submarine earthquake of December 26, 2004 on the west coast of Sumatra, Indonesia. Nearly 300,000 people in three different countries around the Indian Ocean lost their lives.

In deep oceans, a tsunami has a typical length of hundreds of kilometers, a few centimeters height, and travels towards the coast with speeds as high as 500 km/hr. As it starts to climb the continental slope, shoaling effects slow down the wave, shorten the length, and increase its height. Depending on the nearshore topography and its height, it may break on the continental shelf and reaches the coast as a propagating bore. If the wave does not break, it reaches the coast as a steep gradient wall of water. Once the waves reach the shoreline, they break if they have not already broken, and a foamy turbulent bore climbs the dry beach slope with considerable height and speed. Because

of the large height and speed, they are capable of penetrating inland for a large distance. In addition, they have sufficient energy to erode the sediments from the land adjacent to the shoreline and deposit them several hundred meters farther inland. Unlike regular waves, the velocity profile of water particles under tsunamis extends to large depths. In other words, closer to the coast and on the continental shelf, the seafloor feels the propagation of a tsunami on the water surface since the water particles adjacent to the ocean's bottom also move with some velocity. Therefore, tsunamis are "deep nature" waves. They are capable of eroding the sediments from the seafloor, and transporting them up the slope to the coast. Observation of sediments containing microfossils at the coast confirmed the erosion of sediments from the seafloor and their transportation to the coast by tsunamis.

Tsunami generation is difficult to simulate in the laboratory because of the numerous unknowns associated with the complex nature of the generation mechanisms. Moreover, the abrupt and unexpected nature of tsunami generation prevents scientists from acquiring reliable field data to better understand this phenomenon. Tsunami propagation has become better understood following the acquisition of reliable field data during the transoceanic propagation of recent tsunamis (for instance Indian Ocean tsunami of 2004). However, laboratory modeling of tsunami propagation encounters scale difficulties due to the large wavelength and enormous traveling speed. As mentioned earlier, shoaling effects decrease the wavelength and traveling speed of tsunamis drastically as the waves approach the coast. This makes it easier for scientists to simulate the nearshore propagation and coastal impacts of tsunamis in laboratory wave-tanks.

The type of tsunami observed near the coast is a function of its generation mechanism, the nearshore bathymetry, and the tidal level (Ramsden, 1993). Since tsunamis may reach the coast with different profile shapes and propagation characteristics, they manifest different behaviors in their nearshore propagation, inland penetration, interaction with structures and even geomorphological imprints. Therefore, in order to better simulate the nearshore propagation and coastal impacts of tsunamis in laboratory wave-tanks, generation of accurate nearshore tsunami profiles is of high importance to tsunami research. Generation of accurate nearshore tsunami profiles also helps to better verify numerical codes and analytical solutions.

Solitary waves are often used to simulate tsunamis in the laboratory (see Chapter 2). Following the derivation of the wave-paddle trajectory for the generation of solitary waves by piston-type wavemakers in laboratory wave-tanks by Goring (1979), many laboratory studies have been undertaken to investigate tsunami propagation, run-up and coastal impacts (e.g. Synolakis, 1986 for run-up; Ramsden, 1993 for interaction with structures; and many others). Solitary waves generated by the Goring's methodology reach their stable form after a considerable distance of approximately 80 times the water depth following their formation (Guizien and Barthelemy, 2002). Therefore, laboratory studies have been limited to long set-ups on the order of tens of meters. In the derivation of the wave-paddle trajectory, Goring (1979) overlooked the evolving nature of a wave during formation as was previously also pointed out by Synolakis (1990). The main motivation behind the first part of the present study was to achieve more accurate solitary wave profiles in a shorter distance in order to facilitate tsunami research in small set-ups

(see Chapter 3 for set-up details). Therefore, a New methodology that considers the evolving nature of the waves during generation has been developed and verified by a series of laboratory experiments, which is discussed in Chapter 4.

Since tsunamis are generated by an impulsive mechanism, close to the generation zone, their profile contains both elevation and depression components as shown in Fig. 1.1a. Depression components (Fig. 1.1*a*) gradually merge to form a coherent individual depression component (Fig. 1.1*b*) in the profile of a propagating tsunami. Typically, water surface depressions are hydrodynamically unstable in water depths larger than a few millimeters (Korteweg de-Vries, 1895). However, due to the long wavelengths of tsunamis and their enormous traveling speeds, depressions may remain attached to the main hump as the wave propagates across the ocean and reaches the coast. This is especially noticeable in the case of locally generated tsunamis which are closer to the coast, when viscous and dispersive effects do not have enough time to affect the depression profile. In this case, instead of a pure solitary wave, a solitary wave following or leading a depression reaches the coast. The depression is associated with the recession of water along a shoreline and has been recently observed and photographed by eyewitnesses during the Mexican tsunami of 1995 (Borrero et al., 1997). Depending on the position of the depression relative to the elevation, waveforms are called Leading Depression N-waves (LDN) or Leading Elevation N-waves (LEN). There is not a theoretical profile for N-waves, but there are some suggested profiles based on field observations cited in the literature (e.g., Tadepalli and Synolakis, 1994 and 1996; Carrier et al., 2003). However, most of these profiles were suggested to simplify the analytical

calculation and are not necessarily the best fit to the field data. A typical waveform far from the generation zone is shown in Fig. 1.1b.

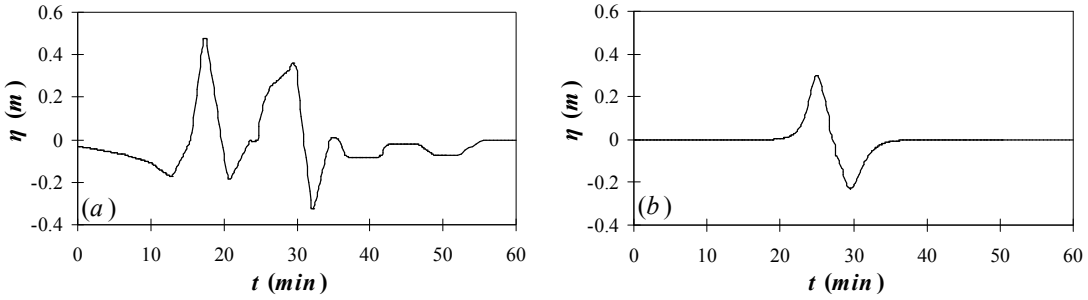

Figure 1.1. Sample tsunami waveform generated by an imaginary submarine earthquake in a rapture zone of 270 *km* long and 70 *km* wide and in water depth of 4 *km* (for details see Geist and Dmowska, 1999). (a) Initial tsunami waveform at the generation zone calculated using elastic halfspace method (Okada, 1985; Kajiura, 1963) (b) Propagated tsunami waveform calculated using the linear long wave theory (Geist and Dmowska, 1999)

Motivated by the recent field observations of water recession along coastlines, in this present study water surface depressions are experimentally studied to develop a fundamental understanding on the propagation characteristics of depressions. Such an understanding is essential to eliminate the critical knowledge gap towards elucidation of coastal impacts of tsunamis. Depressions were generated in the laboratory wave-tank assuming a profile of solitary wave. Evolutions of the depression and oscillatory trailing wave train with distance have been investigated. Details of experiments and discussion of the results have been presented in Chapter 5.

CHAPTER TWO

LITERATURE SURVEY

This chapter comprehensively reviews numerous investigations on the generation of tsunamis in laboratory wave-tanks. As stated earlier, tsunamis may reach the coastal zone in a form of one or a series of solitary or solitary-like waves or bores.

2.1. Solitary and Solitary-like Waves

A solitary wave consists of a single hump of water entirely above still water level with an infinite wavelength (Goring, 1979). Solitary waves were observed by Scottish naval engineer, John Scott Russell, for the first time in 1834 while he was conducting experiments to determine the most efficient design for canal boats. Following this observation, the first attempt to generate solitary waves was undertaken by Russell in 1845 in a 10 *m* tank. He generated solitary waves in two different ways. In the first set of experiments, he generated a solitary wave by dropping weights in one end of the tank. Once the weight is dropped into the water, splashing occurs. The wave leaves the splashing zone and after some distance, a solitary-like wave forms and travels toward the other end of the tank. In the second set of experiments, he generated solitary waves by removing a barrier and releasing large amount of water from one end of the tank. The released water first moves at the water surface like a wall of water and then gradually reshapes into a solitary wave. In this second set of experiments, Russell unknowingly applied the theory by Hammack and Segur (1974), which states that from any net positive

disturbance in a water surface, one or a series of solitary waves followed by dispersive oscillatory trailing waves emerge.

It was after mid-20th century that scientists realized the importance of Russell's observations in the complicated problem of impulsive waves. Motivated by the observation of surface waves generated by underwater explosions, Johnson and Bermel (1949) carried out similar experiments to those performed by Russell (1845). They dropped weighted blocks with a range of weights and circular discs with various diameters and weights into a 35 m × 20 m × 0.6 m hydraulic basin. Experiments were conducted on both horizontal and sloped bottoms. Maximum wave heights were measured at different distances from the splashing point.

Later, Wiegel (1955) performed a series of experiments to generate solitary waves to investigate the generation of gravity waves by underwater landslides. Initially, underwater landslides were modeled using a steep pile of coarse sediments lying on a metal sheet. Pulling the sheet from under the pile destroyed its equilibrium and caused the slide to move under the water. However, the slide originated by this method was not effective enough to create realistic waves in terms of amplitude. In the next attempt, coarse sediments were piled behind a vertical plate in a channel. By lifting the plate, the coarse sediments were released and the slides were generated. However, the new method did not improve the order of magnitude of the waves' amplitude generated by the previous method. Consequently, as the final attempt, bodies of different shapes, sizes and weights were allowed to drop vertically or to slide down inclines of different angles in water of various depths from several heights above the bottom, yet always below the

water surface. While the objective of experiments was not generation of solitary waves, recording of water surface elevation at different locations along the tank demonstrated the gradual deformation of generated waves into a solitary wave profile along the wave-tank. Similar experiments to those performed by Johnson and Bermel (1949) to model impulsive waves generated by underwater landslides or subaerial landslides have been reported by many investigators such as Prins (1958), Kamphuis and Bowering (1970), Singerland and Voight (1979), Heinrich (1992), Watts (1997, 1998), Grilli and Watts (1999, 2001, 2005), Enet et al. (2003), Walder et al. (2003, 2006), and Sue et al. (2006).

The use of wave paddles to generate impulsive waves originated with laboratory experiments of Daily and Stephan (1952). In order to simulate earthquake generated tsunamis, they moved the tank bottom vertically by means of a hydraulic jack resembling a tectonic plate. Later, Hammack (1972) used the same method, but he controlled the hydraulic mechanism of wave generation system with a micro-computer. The trajectory of the moving part of the tank bottom was determined using the basic wavemaker theories developed by Havelock (1929) and Kennard (1949). A piston-type wavemaker was used for the first time by Hall and Watts (1953) to generate impulsive waves. They used a mechanical system to move the wave paddle horizontally. The purpose of the experiments was not solitary wave generation, but generation of impulsive waves in order to visualize the run-up process and measure the maximum run-up height on a beach slope. However, they unintentionally generated solitary waves by moving the wave paddle horizontally. This method was used afterwards by Camfield and Street (1969) to generate solitary waves using horizontal movement of the wave paddle. The motion of

the wave paddle was controlled by a hydraulic system which was commanded from a micro-computer. The trajectory of the wave paddle was determined using the basic wavemaker theory. During 1960s and 1970s, solitary waves were most often generated by less expensive methods such as sudden release of an air valve on a vacuum tank that held a prescribed amount of water (e.g., Kishi and Saeki, 1966).

Following the laboratory experiments carried out by Camfield and Street (1969), Goring (1979) attempted to generate more accurate solitary waves by defining the wave paddle trajectory for a given solitary wave profile. This solitary wave generation theory assumes that the horizontal component of the water particle velocity adjacent to wave paddle is equal to the wave paddle velocity:

$$\frac{d\xi}{dt} = \bar{u}(\xi, t) \tag{2.1}$$

where ξ is the wave paddle position, t is the time and $\bar{u}$ is the horizontal water particle velocity adjacent to the wave paddle. Horizontal water particle velocity is assumed to be constant throughout the depth and equal to the depth-averaged velocity which is derived from the continuity equation by Svendsen (1974) for long waves of permanent form:

$$\bar{u}(\xi, t) = \frac{c\,\eta(\xi, t)}{h + \eta(\xi, t)} \tag{2.2}$$

where η is the free surface elevation above still water level, h is the water depth at the paddle and c is the wave celerity. To generate solitary waves, Goring (1979) used Boussinesq (1871)'s first-order solution for the solitary wave profile:

$$\eta(\xi, t) = H \sec h^2\left(k(ct - \xi)\right) \tag{2.3}$$

where H is the wave height, k ($=\sqrt{3H/4h^3}$) is the boundary decay coefficient or solitary wave number, and $c = \sqrt{g(h+H)}$. Eqns. 2.1 through 2.3 yields to the trajectory of the wave paddle in the following implicit form:

$$\xi(t) = \frac{H}{kh}\tanh(k(ct-\xi)) \tag{2.4}$$

This implicit wave paddle trajectory equation can be solved numerically (e.g., using Newton-Ralphson method). From Eqn. 2.4, the total stroke length of the wave paddle, S, can be calculated as $2H/kh$. Ideally, the total duration of the wave paddle, T, approaches infinity. However, to make it practical, Goring assumed that after 99.9% of the total stroke length, the wave profile is completely generated, and therefore the total duration of the wave paddle was calculated as $T = 7.8/kc + S/c$. Goring (1979) generated solitary waves in different depths of water and for relative wave height, $\varepsilon = H/h$ ranging from 0.1 to 0.7. He reported that the greater the ε, the less agreement between the generated wave height and the theoretical (i.e. aimed) wave height. The generated wave height is reported much smaller than the aimed wave height. The deviation from theory was not limited to the wave height but also included the boundary shape and the celerity of generated wave. Goring reported severe damping for the generated Boussinesq-type waves. He added that this amount of decay can not be explained by frictional damping only. For greater values of ε, he observed greater damping. In terms of change in profile shape, Goring (1979) reported larger change near the wave generator, but as the wave propagates farther away from the generation zone, the rate of wave profile change decreases drastically. Solitary waves generated by piston-type wavemakers are followed by dispersive oscillatory trailing waves. Goring (1979) reported the trailing wave

amplitude in a range of 6% to 12% of the solitary wave height. He demonstrated experimentally that increasing the total duration of wave paddle motion by 10% can reduce the trailing wave's amplitude significantly. Goring's method have been commonly used in laboratory studies to generate solitary waves and specifically to investigate tsunami propagation, run-up and coastal impacts (e.g. Synolakis, 1986 and 1987; Zelt, 1986; Ramsden, 1993; Li, 2000; Li and Raichlen, 2001; Jensen et al., 2003).

Recently, Guizien and Barthelemy (2002) conducted a series of experiments in a 36 *m* long, 0.55 *m* wide and 1.2 *m* deep wave-tank that is equipped by a piston-type wavemaker, and they generated solitary waves using the method developed by Goring. In addition to the Boussinesq's solitary wave solution that was used by Goring (1979), Guizien and Barthelmy used Rayleigh's (1876) solution along with first- and second-order shallow water solutions by Korteweg de-Vries (1895) (1^{st} and 2^{nd} order KdV solutions) to define the wave paddle trajectory. Note that Rayleigh's solution differs from Boussinesq's solution only by the definition of the solitary wave number, k, which is defined as $(3H/(4h^2(H+h)))^{1/2}$. Guizien and Barthelemy conducted experiments in 20 *cm* and 30 *cm* depths of water for various values of relative wave height, ε, ranging from 0.05 to 0.6. They numerically solved Eqns (2.1) through (2.3) simultaneously and by linearization of the numerical results, proposed the following explicit solution for the trajectory of the wave paddle based on Rayleigh's profile:

$$\xi(t) = \frac{H}{hk}\frac{h\tanh(kct)}{h + H\left(1 - \tanh^2(kct)\right)} \tag{2.5}$$

Their laboratory experiments showed that generated waves based on Rayleigh's solution are more accurate in terms of wave height, profile shape and celerity compared to those

generated based on Boussinesq's solution. 1st and 2nd order KdV solutions led to less accurate solitary wave generation. In addition, they reported that damping of the Rayleigh-type waves seems explainable by frictional damping. They also described that Rayleigh-type waves achieve their permanent form in a shorter distance, approximately 20 times water depth compared to Boussinesq-type waves which achieve their permanent form after approximately 80 times water depth. Guizien and Barthelemy related this behavior to the better description of k in Rayleigh's solution that is suggested by the numerical solution of Byatt-Smith (1970, 1971).

Jensen et al. (2003) used the Goring's method with Boussinesq's profile to generate solitary waves in order to study tsunami run-up. For high-amplitude solitary waves, they argued that long wave theory is no longer valid. Consequently, they used numerical solution of Tanaka (1986) rather than the first-order approximate solution of Boussinesq (1871). However, they incorporated the solitary wave profile in the same Eqn. 2.2 to find the depth-averaged velocity values. Tanaka's numerical solution provides larger k values and consequently smaller stroke length compared to Boussinesq's and Rayleigh's solutions. Since Jensen et al. (2003) had a limitation on maximum stroke length of the wave paddle, the use of Tanaka's solution allowed them to generate steeper solitary waves. However, as mentioned earlier, Eqn. 2.2 was derived based on long wave theory assumptions. Therefore, it is not evident whether the use of Eqn. 2.2 with any higher order definition of solitary wave profile, such as numerical solution of Tanaka, improves the wave generation process or not.

2.2 Bores

In many circumstances, solitary-like waves break offshore or on dry land and form a turbulent bore which continues climbing up the beach until it is overtaken by another bore or drawn back under gravity.

There have been several laboratory investigations to generate turbulent bores resembling breaking tsunamis. Extensive laboratory experiments were reported about bore generation and run-up by Miller (1968). Miller used a vertical paddle to generate bores; the piston moved at constant speed and stopped suddenly after a distance. Later, Yeh et al. (1989) performed in-depth laboratory investigations on generation and run-up of fully-developed and undular bores on an initially dry beach. A bore was generated by lifting a thick aluminum plate which separates the stationary water on the beach from the deeper water behind it. Recently, Chanson et al. (2002), assuming that tsunami bores are similar to plunging jets in nature, generated bores by the vertical release of a known water volume. Water was released through a rectangular, sharp-crested orifice with 70 *mm* by 750 *mm* cross-sectional area at one end of the channel, similar to a dam break surge. While the method in generating bores was innovative, further investigations are needed to demonstrate the adequacy of the aforementioned assumption for the accurate simulation of the characteristics of the run-up process (Chanson et al., 2002).

In one of the first analytical attempts to simulate bore run-up, Whitham (1958) proposed that bore propagation was governed by the known hydrodynamic principles immediately behind it. Applying this statement, a widely accepted analytical solution for the

propagation of bores was presented by Meyer and his associates during the 1960s which is summarized by Meyer and Taylor (1972). Shen and Meyer (1963) transformed Nonlinear Shallow Water (NLSW) equations into a set of linear shallow-water equations by using canonical variables. They showed that the shoreline position is insensitive to other wave motions and only governed by gravity. As the bore approaches the shoreline, the bore height decreases and eventually will become zero at the new shoreline (Whitham, 1958; Ho and Meyer, 1962).

2.3 Water Surface Depressions and N-waves

The profile shape and amplitude of the water surface deformation in the vicinity of the generation zone is dominated by the magnitude and pattern of the seafloor displacement. By considering the Earth's crust as an elastic halfspace, Okada (1985) derived a set of analytical expressions for the seafloor dislocations due to inclined shear and tensile faults. For the rise time of most earthquakes, displacement of the seafloor can be considered instantaneous relative to the propagation speed of tsunamis. Therefore, the water surface profile in the generation zone mimics the vertical component of the seafloor displacement (Kajiura, 1963). In other words, by assuming that the ocean is an incompressible layer of liquid over an underlying elastic halfspace, the seafloor dislocation field can be transferred directly to the water surface by applying appropriate attenuation factors. Starting with the three-dimensional Green's function for water motion in an ocean of finite depth, Kajiura (1963) demonstrated that the effect of attenuation on the initial water surface disturbance can be approximated by applying a

reduction factor of 1/cosh(kh) to the vertical seafloor displacement field, where k is the wave number, and h is the water depth.

The initial disturbed water surface, which lies very close to the seismic faulting zone, is irregularly composed of different elevation and depression parts, thus it is often called "the splashing zone". The initial water surface profile predicted by numerical simulations based on the aforementioned elastic halfspace theory is shown in Fig. 1.1a. The elevation and depression parts in the wave field gradually merge as the generated disturbance propagates radially. If there is enough distance from the tsunami source to the coast, the wave field eventually reshapes into a so-called "N-wave" profile including a single elevation and a single depression part. Depending on the relative position of the elevation and depression components, two types of N-waves including Leading Elevation N-wave (LEN) and Leading Depression N-wave (LDN) are possible. This is confirmed by numerical simulation of wave propagation based on long wave theory as shown in Fig. 1.1b and also several tidal gauge recordings at the coastline during tsunami events (e.g., Borrero et al., 2005).

Since the first observation of a solitary wave on the water surface by Russell (1844) and supporting analytical studies (e.g., Boussinesq, 1871; Rayleigh, 1878; Korteweg and de-Vries, 1895 and many others) solitary waves of elevation (above still water level) have been widely studied experimentally (e.g. Hammack and Segur, 1974; Goring, 1979; Guizien and Barthelemy, 2002), as well as analytically (e.g., Benjamin, 1972; Byatt-Smith and Longuet-Higgins, 1976; Tanaka, 1986). It has been emphasized by Korteweg

and de-Vries (1895) that solitary waves can be in the form of both elevation (positive; i.e. above still water level) and depression (negative; i.e. under still water level). In the long wavelength limit when the gravitational force is dominant, only elevation solitary waves can be observed. However, for shorter wavelengths, when surface tension is no longer negligible, capillary effects have a drastic influence on the water surface waves and depression solitary waves can also be observed (Falcon et al., 2002). In fluid mechanics, the Bond number is a dimensionless number expressing the ratio of body forces (often gravitational) to surface tension forces and defined as $\mathrm{Bo} = (l_c/h)^2$, where $l_c = \sqrt{\sigma/\rho g}$ is the capillary length of water, and h is the water depth. In the equation for capillary length of water, σ is the water surface tension. When $0 < \mathrm{Bo} < 1/3$, elevation solitary waves are stable form of disturbance when $\mathrm{Bo} > 1/3$, depression solitary waves could be observed (Korteweg and de-Vries, 1895; Falcon et al., 2002). Assuming the density of tap water, ρ, as 1.0×10^3 kg/m^3, the water surface tension, σ, equal to 0.0728 N/m^2, and the dynamic viscosity of water, μ, as 1.0×10^{-3} $N.s/m^2$, the capillary length of seawater, $l_c = \sqrt{\sigma/\rho g}$, is calculated as 2.7 *mm*. The Bond number, $\mathrm{Bo} = (l_c/h)^2$, for 30 *cm* water depth is then calculated as 8×10^{-5} (notice that the value calculated for Bond number is for 30 *cm* water depth of the wave-tank and in deep oceans by increasing the water depth, the value gets very minuscule). Therefore water surface depressions are hydrodynamically unstable especially in large water depths such as in the ocean.

As the N-wave shown in Fig. 1.1b propagates toward the coast, the depression stretches out and its amplitude attenuates rapidly with distance. Attenuation of the trough is due to viscous dissipation and nonlinear dispersion. Moreover, the depression part propagates

with a lower celerity compared to the elevation part closer to the coast (Korteweg and de-Vries, 1895). Consequently, if there is enough propagation distance for an LDN-wave, the depression part will be overtaken by the elevation component due to the lower celerity. However, when the seismic source of undersea earthquake is closer to the coast, there will not be enough propagation distance for the elevation component to exterminate the trough and both elevation and depression parts of the wave will reach the coast. While it is shown theoretically that stable water surface depressions will not be formed on the ocean surface, it does not mean that they should be neglected. Water surface depressions are unstable in deep oceans and in laboratory wave-tanks in water depths of larger than 1 *cm* (Korteweg de-Vries, 1895). However, they are still capable of propagating large distances while attenuating drastically with distance.

In deep oceans, depressions are very long and only a few centimeters in amplitude. However, water depth decreases near the coast and thus, the relative amplitude of the trough ($\varepsilon_t = a_t/h$; a_t - maximum trough amplitude) increases. Tidal gauge recordings for major tsunami events are listed in Table 2.1. Gauge stations listed in Table (2.1) are coastal tidal gauges and do not include those installed close to the islands. There is no reference regarding the water depth at the position of gauges. However, since they are close to the coastline, the water depths at coastal gauge stations are always assumed to be less than 10 *m* (see for example Satake, 1995).

Table 2.1 Depression amplitude recorded by gauges during major tsunami events

Tsunami Event	Gauge Station	Distance from the source (km)	Depression Amplitude (m)	Reference
Indian Ocean, 2004	Kurabi	~700	0.4	Tsuji et al. (2006)
	Colombo, Sri Lanka	~2000	1.4	Rabinovich and Thomson (2007)
	Salalah, Oman	~4500	1.1	
	Lamu, Kenya	~5500	0.5	
	Paradip, India	~1900	1.2	
	Vishakhapatnam, India	~1600	1.1	
	Chennai, India	~1600	1.6	
	Neendakara, India	~2200	1.1	
	Tuticorin, India	~2000	1.0	
	Kuraburi, Thailand	~850	1.4	
	Ranong, Thailand	~800	1.4	
	Trang, Thailand	~750	1.25	
	Belawan, Indonesia	~300	0.93	
	Sibolga, Indonesia	~450	2.46	
Kii Peninsula, 2004	Uragami, Japan	~320	0.75	Satake et al. (2005)
	Kushimoto, Japan	~300	0.65	
Hokkaido, 1993	Wajima, Japan	~550	0.5	Nagai et al. (1996)
Alaskan, 1964	Alameda, CA	~3500	1.0	Magoon (1966)
	San Francisco, CA	~3500	1.3	
Chilean, 1960	Alameda, CA	~9500	0.4	Magoon (1962) & Berkman and Symons (1960)
	San Francisco, CA	~9500	0.45	

Since the approaching N-wave has a steeper water surface gradient and consequently a larger inertia, it may climb up the beach to higher points with higher velocities during run-up. Similarly, the wave may draw back more rapidly and further offshore during run-down compared to a corresponding solitary wave with the same elevation height (Tadepalli and Synolakis, 1996; Carrier et al., 2003). Since the velocity of run-up and run-down increase, the net slamming drag force exerted on coastal structures will increase as well (Carrier et al., 2003; Yeh, 2006). Moreover, pronounced geomorphological imprints including stronger erosion and sediment transport are expected. These N-waves are believed to be responsible for several documented observation of shoreline recession during tsunami events (e.g., Borrero et al., 1997 for 1995 Mexican tsunami). Being aware of higher coastal impacts of N-waves, one may propose that N-waves are also responsible for inaccurate and underestimated results of prevailing solitary wave-based numerical or analytical models. On the other hand, profound doubt in hydrodynamic stability of N-waves (especially in long distances) and uncertainties about inferring the initial N-wave profile from uplift and subsidence magnitudes of seafloor deformation are limiting laboratory modelers in studying N-waves. Consequently, numerical modelers mainly utilize solitary waves as initial conditions and apply large amplification factors to fit their numerical results to run-up field measurements. To the writer's knowledge, there is no or only a few unpublished reports of experimental investigations on the generation, propagation or coastal impacts of N-waves. However, there have been a few analytical studies proposing a profile for N-waves and solving the run-up equations for both solitary waves and N-waves (e.g., Tadepalli and Synolakis, 1994 and 1996; Carrier et al., 2003).

Carrier et al. (2003) assumed the following profile for LDNs and LENs as tsunamis:

$$\eta = a_1 \exp\left[-k_1(x-x_1)^2\right] - a_2 \exp\left[-k_2(x-x_2)^2\right] \tag{2.6}$$

where a_1 and a_2 are elevation and depression heights respectively. x_1 and x_2 are positions of a_1 and a_2 along the x-axis respectively assuming the x-axis has an arbitrary origin. k_1 and k_2 are constants and define the length and boundary shape of elevation and depression parts respectively. By introducing α as the beach slope and L as any horizontal length scale such as the fault width, later Yeh (2006) represented this profile in dimensionless form as:

$$\eta' = a_1' \exp\left[-k_1'(x'-x_1')^2\right] - a_2' \exp\left[-k_2'(x'-x_2')^2\right] \tag{2.7}$$

where $\eta' = \eta/\alpha L$, $x' = x/L$, $x_1' = x_1/L$, $x_2' = x_2/L$, $a_1' = a_1/\alpha L$, $a_2' = a_2/\alpha L$, $k_1' = L^2 k_1$ and $k_2' = L^2 k_2$ are dimensionless substitutes. Based on this profile, Carrier et al. (2003) showed that the maximum flow velocity for predominately negative waves (i.e., larger depression parts than elevation parts) occurs during run-up while the maximum flow velocity for predominantly positive waves (i.e., larger elevation parts than depression parts) occurs during run-down. This implies that for a predominantly positive LDN, the maximum momentum flux (force) occurs immediately after the maximum penetration, before flow reversal, and in the offshore direction. For a predominantly negative LDN, the maximum momentum flux occurs immediately after flow reversal and in the onshore direction. Therefore, the maximum force exerted on coastal structures will take place at the extreme draw-down location, regardless of the specifics of the LDN.

Tadepalli and Synolakis (1996) proposed the following general profile for both solitary waves and N-waves:

$$\eta = \varepsilon H\left(x - X_2\right)\sec h^2\left[k\left(x-\theta\right)\right] \tag{2.8}$$

In this equation, η is wave amplitude, $k = \sqrt{3H\lambda/4}$, $\theta = X_1 + ct$, $L = X_1 - X_2$, $c = 1$, and λ is a steepness parameter. X_1 and X_2 are arbitrary constants which defines the length and shape of the profile. $\varepsilon < 1$ is a scaling parameter defining the crest amplitude introduced only for reference to ensure that the wave height in Eqn. 2.8 is H. Tadepalli and Synolakis (1996) added that ε can be chosen in such a way that Eqn. 2.8 fits any desired surface profiles inferred from the field observations. H and the wavelength of the profile in Eqn. 2.8 are substituted from vertical and horizontal measures of the ground deformation, respectively. Tadepalli and Synolakis (1994) analytically showed that an LEN runs up higher than a solitary wave with the same elevation height but less than a similar LDN. They explained this larger run-up height by the larger inertia produced by a steeper water surface slope in an approaching LDN compared to an LEN. By a similar discussion, they reasoned the higher run-down calculated in the case of an LEN.

In order to examine the stability of an LDN during transoceanic propagation, Tadepalli and Synolakis (1996) solved KdV equations for the N-wave profile of Eqn. 2.8. For an initial height-to-depth ratio of 0.01, they showed that tsunamis with LDN profiles will remain unchanged for distances over 4000 depths while for a more realistic initial height-to-depth ratio of 0.001, this value will be 2000 depths. Moreover, they showed that run-up values of LDNs increase as the ratio of trough-height to crest-height increases. Finally, they conclude that the orientation of the subduction zone, the direction of the

slip, and the maximum sea-bottom displacement significantly change the shape of the generated N-Waves. Thus, numerical and experimental simulations based on solitary waves do not necessarily provide us with the maximum run-up heights of the tsunamis as observed in 1992 Nicaraguan event (Satake, 1994 and 1995) and 1993 Flores Island event (Yeh et al., 1993).

While N-waves seems to be only a subject of a few unreported experimental studies recently, there are a series of laboratory experiments reported by Hammack (1973) and Hammack and Segur (1974, 1978) about the generation of complex waveforms with different elevation and depression components. They also reported the generation and propagation of pure elevation and pure depression waves. Different waveforms were generated in order to determine whether a solitary wave would emerge from the waveform in the far field, and if so, it was desired to understand the factors behind the profile shape and propagation.

CHAPTER THREE

EXPERIMENTAL SET-UP AND TECHNIQUES

This chapter is organized into two principle sections: Experimental Setup and Instruments. The Experimental Setup section contains information regarding the wave-tank and wave generation system whereas the Instrument section includes information referencing equipments that used to acquire experimental data including data acquisition system, wave gauges, digital video camera, Laser Displacement Sensor (LDS), and high-speed video camera.

3.1 Experimental Set-up

Wave-Tank

Experiments were conducted in a 12 *m* long, 0.6 *m* wide and 0.6 *m* deep wave-tank located at the Flow Physics Laboratory of the Civil Engineering Department of Clemson University. The tank is constructed of eight identical 1.5 *m* steel-framed modules. The sidewalls and bottoms of each module are made of Plexiglas panels measuring 1.5 *m* long, 0.6 *m* wide, and 0.5 *cm* thick. Tank bottom is elevated 1 *m* from the ground to ease the visualizations from the sides and bottom. The carriage rails, made of 1.5 *cm* diameter stainless steel, are bolted at 1 *m* intervals to the top flanges of the tank sidewalls. There is a small clearance of 1 *cm* between the rails and top flanges.

To avoid the problem of leakage at the tank bottom and sidewalls, the Plexiglas bottom of the wave-tank is sealed by a waterproof chemical sealant which is extended to the height

of 10 *cm* on both sidewalls. Since the waves should be generated in stable and quiescent water and in order to reduce reflection, and thereby, the time between each experiment, an artificial porous beach was placed at the other end of the tank, opposite of the wavemaker. In order to reduce the reflection of the waves from the wave paddle and the wall behind the wavemaker, plastic fiber meshes is installed behind of the wave paddle as a wave absorber. A schematic of the wave-tank is shown in Fig. 3.1.

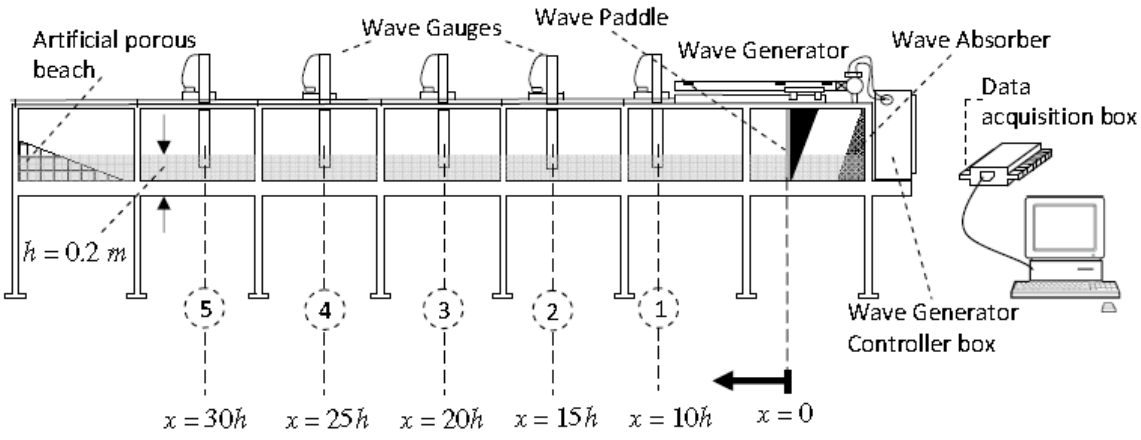

Figure 3.1 Schematic of the experimental set-up. Numbers 1 to 5 represents the position of wave gauges in equal steps of 1 *m*.

The wave generator, which was designed and constructed for this study, consists of a vertical aluminum plate which is moved horizontally in a defined trajectory by means of an electrical servo-system. The system accepts a programmed input voltage and converts this input electrical signal into a displacement. The displacement-time history or the "trajectory" of the wave paddle movement is linearly proportionate to the voltage-time history of the input signal.

Wave Generation System

The wave generation system for this study is comprised of three main parts; a mechanical module consists of a vertical wave plate and a linear actuator system, a power module consists of a servo-electrical motor, and a controller module. A picture of the wave generation system is shown in Fig (3.2).

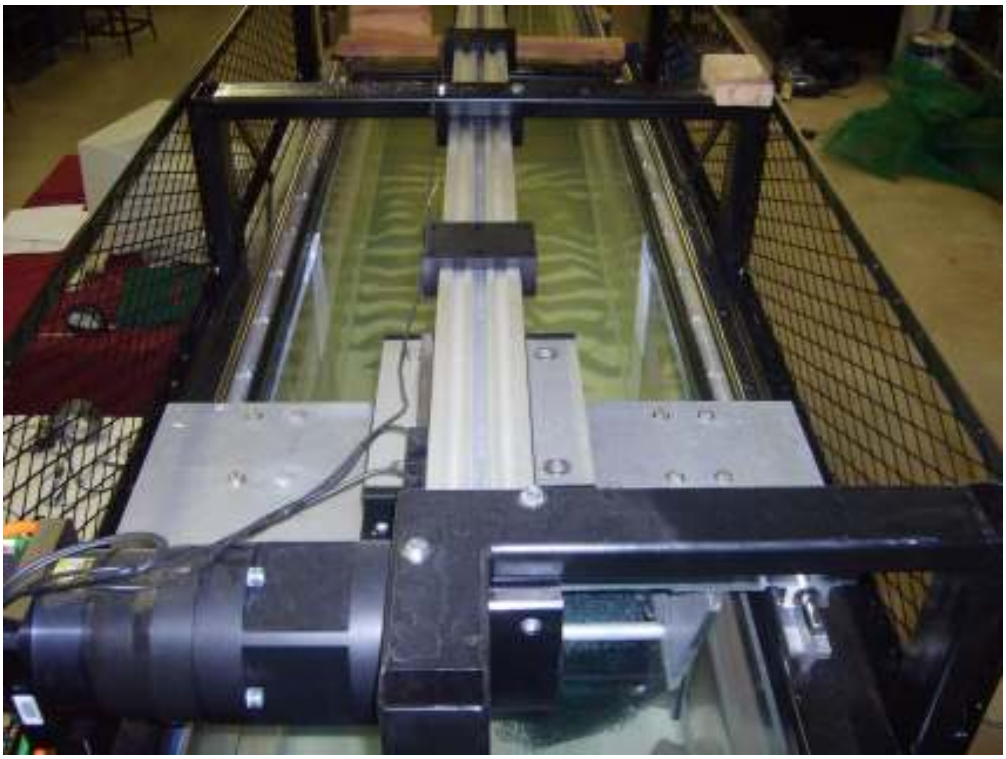

Figure 3.2 Piston-type wavemaker at Flow Physics Laboratory of Clemson University

The mechanical module of the wave generation system consists of a precise linear actuator system with a position resolution of 1 μm, a vertical wave paddle, a carriage-rail

system for the movement of the wave paddle, and a supporting steel frame. The linear actuator system consists of a 30 *cm* long, 20 *cm* wide, and 15 *cm* thick aluminum cubical slide which travels on a linear aluminum guide of 2 *m* long. The linear actuator system has a maximum stroke length of 1.5 *m* and is capable of reaching a maximum velocity of 1.5 *m/s* and a maximum acceleration of 10 m/s^2. It is secured by the steel frame at the top of the first module of the wave-tank that is bolted into place. The vertical aluminum wave plate is bolted from the top to the center of the actuator slide by means of a circular shaft to minimize the resistant moment on the slide motion. To avoid the potential leakage around the wave paddle, the sides of the paddle are sealed with flexible rubber membranes.

Once the theoretical trajectory of the wave paddle is calculated, it is transferred in terms of a digital voltage signal from the operator computer to the controller through a LabView code. By means of a built-in D/A converter, the digital voltage is converted to an analogue voltage signal readable by the servo-electrical motor. The analogue signal is stored by the controller in the memory and once the controller is commanded from the operator computer to run the trajectory, the analogue signal is sent to the servo-electrical motor. The Servo-electrical motor is a shaft-driven motor, in which the shaft rotation is proportionate to the displacement of the wave paddle. Once the analogue voltage signal is received by the servo-electrical motor, it is converted to the time-radial displacement history of the shaft to maintain the proposed trajectory of the wave paddle.

To estimate the accuracy of the wave generation system in operation, the actual movement of the wave paddle as a response to the calculated trajectory is recorded by

using a Laser Displacement Sensor (LDS) with a precision of 0.01 *mm*. An example of the comparison between a programmed and an actual trajectory and velocity of the wave paddle is shown in Fig. (3.3a & b). A time lag of approximately 0.05 *s* between the programmed and actual motion is recognized which is normal and is attributed to the time elapsed in communication between the linear actuator system and the electrical servo-system. Apart from this, the actual motion shows an excellent agreement with the programmed motion. Repeatability of the wave generation system is examined by recording the movement of the wave paddle for 20 different runs of generating the same solitary wave profile. Errors in the movement, ξ_{error}, and velocity, u_{error}, of the wave paddle are presented in Fig. (3.3 c & d). Errors were always below 2% for both movements and velocities.

3.2 Instruments

Data Acquisition System

The USB data acquisition interface from National Instrument model NI-6009 is used to acquire voltage signals from wave gauges, and Laser Displacement Sensor (LDS). The interface includes 16 digital input channels, 8 analogue input and 2 analogue output channels with frequency response of 14,000 *Hz*. The LabView software is used to communicate with the data acquisition interface and store the data to computer.

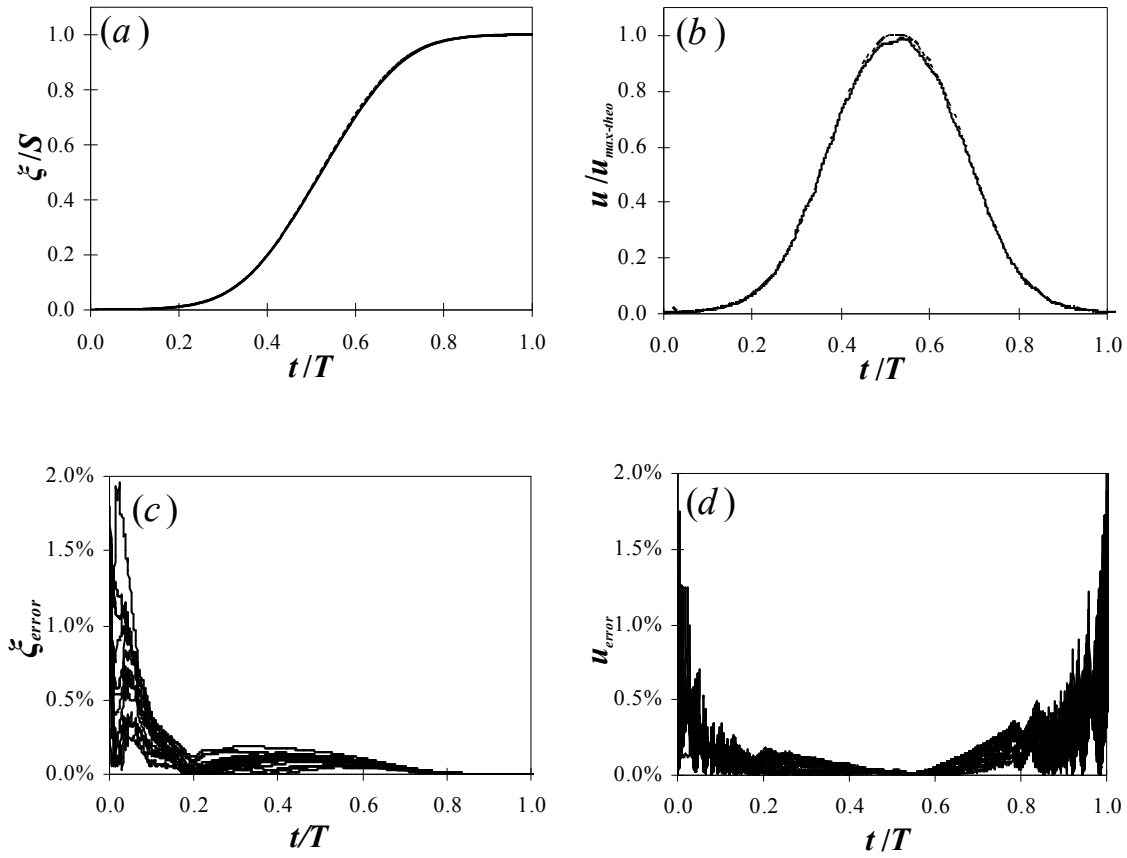

Figure 3.3 Accuracy and repeatability of the wave generator. (*a*) comparison of the theoretical trajectory of the wave paddle (- - -) and the actual trajectory of the wave paddle recorded by LDS (——); (*b*) comparison of the theoretical velocity of the wave paddle (- - -) and the actual velocity of the wave paddle calculated based on LDS measurement (——); (*c*) percent error in the actual trajectory of the wave paddle recorded by LDS for 20 different runs of the same solitary wave profile; (*d*) percent error in the actual velocity of the wave paddle calculated based on LDS measurement for 20 different runs of the same solitary wave profile. (all panels are for a solitary wave with 12 *cm* amplitude in water depth of 20 *cm* ($\varepsilon = 0.6$) based on Rayleigh's solution and generated using Goring methodology.)

Wave Elevation Data Recordings

WG-50 Capacitance wave gauges from RBR Company are used to record the water surface elevation at different sections along the wave-tank as a function of time. The wave gauge consists of a stainless steel bracket-shape frame and a plastic-sealed stainless wire. A controller box provides the necessary voltage for the function of the wave gauge. The wave gauge functions as a capacitor, in which the steel frame and plastic-sealed steel wire are two conductors and the material between these two, either air or water, performs as a dielectric. The amount of electricity stored between the steel frame and plastic-sealed steel wire is linearly proportionate to the conductivity of the dielectric. When the wave gauge is out of water, air is the dielectric between the two conductors, which has the least amount of conductivity. However, in the water, by having the water as a partial dielectric, the conductivity of the capacitor changes by the elevation of the water between two conductors and therefore the amount of electricity stored in the capacitor is changing by time. The amount of electricity stored between the conductors is proportionate to the elevation of the water surface between the two conductors.

The wave gauge measures the stored voltage and transfers it to the controller box. The controller box transfers the stored voltage to the data acquisition system and then a LabView code stores the time-history of the voltage to the operator computer. Output voltage of the wave gauge is between -5, which corresponds to a zero water elevation, and +5, which corresponds to 1 *m* water elevation between the conductors. The time history of the water surface elevation is extractable from the recorded time-history of the output voltage.

Wave gauges are not accurate enough to record the waveforms of smaller than a few centimeters in amplitude. Therefore, in order to measure the small amplitude water surface depressions in water depth of 6 *cm* and 15 *cm*, a digital video camera has been used to record a video of the water surface fluctuations at different sections along the wave-tank. The recorded video is then digitized into a series of high quality images. Knowing the time interval between each image, the profile of the water surface depression is extracted by processing each image and counting the pixels.

Laser Displacement Sensor (LDS)

A Laser Displacement Sensor (LDS) from Keyence Company (model #LK-G502) is used to check the accuracy and repeatability of the wave generator. The LDS measures the distance by emitting a laser beam that reflects off any solid surface within its measurement range. The sampling rate of the LDS can be adjusted to maintain the required resolution starting 100 samples per second. The measurement range of the LDS is between 25 *cm* and 1 *m*. The device can be used stand alone by using a software provided by the Keyence Company, or can be connected to the USB data acquisition interface to acquire the distance in terms of voltage. The output voltage is between -10 and 10 V and is linearly proportionate to the measured distance. It can be calibrated for any desired range between 25 *cm* and 1 *m*. In the present study is was calibrated such that the distance of 25 *cm* and 1 *m* correspond to -10 V and 10 V respectively.

High-speed Camera

A high-speed high-resolution CCD camera from Fastec (model, Troubleshooting) is used to visualize the wave paddle movement. The camera has an adjustable frame rate starting from 125 frames per second (fps) up to 1000 fps. In addition, the shutter speed is adjustable from 1X up to 20X. The user can choose between 6 different resolutions and window sizes. Different lenses can be connected to the camera to provide an appropriate window size and resolution.

CHAPTER FOUR

LABORATORY GENERATION OF SOLITARY WAVES

A New methodology for solitary wave generation by considering the evolving nature of the wave during the generation process is presented in this chapter. The proposed methodology is examined by conducting a series of experiments in the wave-tank (see Chapter 3.1) located in the Flow Physics Laboratory of Clemson University . Solitary waves were generated using both the new and the traditional (i.e., Goring methodology, see Chapter 2 for an overview) methodologies. Waves generated using the Goring methodology served as a benchmark to assess the performance of the New methodology. Generated waves are compared in terms of profile shape (wave height, boundary shape, trailing waves), change in profile shape and amplitude attenuation, establishment rate, and celerity.

4.1 Wave Generation Theory

In order to generate the solitary waves with desired characteristics in the wave-tank, the time-history of the wave paddle motion (i.e., wave paddle trajectory) is required.. In this section, the derivation of the paddle trajectory for the proposed solitary wave generation methodology is presented.

As alluded to by Synolakis (1990), Goring methodology does not consider the unsteady nature of the solitary wave generation process. It rather assumes that a solitary wave of permanent shape forms even during the generation stage. However, in our New

methodology, we consider the evolving nature of the generated solitary wave during the generation stage. It is assumed that as the wave-paddle moves horizontally and pushes the water column out in front, a small surge forms at each instant. These small surges pile up to eventually form the smooth profile of the proposed solitary wave. During the wave profile generation, the evolving/forming wave does not propagate with the constant celerity of the stable solitary wave as it is assumed in Goring methodology. It instead propagates with a celerity that changes with time, $c_u(t)$ [henceforth, referred as "unsteady celerity"]. Therefore, there are two unknowns to be determined when calculating the wave paddle trajectory: $\overline{u}(t)$ [horizontal water particle velocity adjacent to the wave-paddle or equally wave-paddle velocity, see (1)] and $c_u(t)$. To determine these two unknowns at each instant of the paddle motion, mass and momentum conservation equations must be solved.

The selected control volume (CV) for our analysis is illustrated in Fig. 4.1. In this schematic and to maintain clarity, only the initial surge formed by the push of the wave paddle is shown. The water column pushed by the wave paddle enters the control volume through the control surface (CS) indicated as 1 with a depth-averaged velocity of $\overline{u}_1$, and the fluid leaves the control volume through CS2 that is far away from the solitary wave generation zone with a depth-averaged velocity of $\overline{u}_2$. This initial surge of height $\eta(t_1)$ propagates with a celerity of $c_u(t_1)$ over the water depth of h [subscripts for time, t, denotes the instant of time].

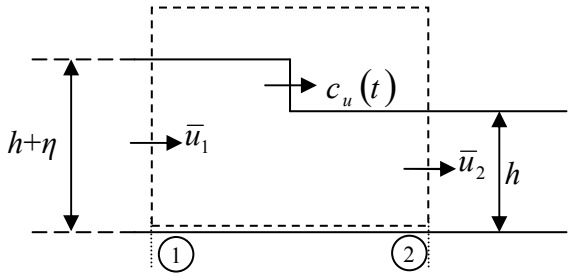

Figure 4.1 Definition sketch of parameters. Dashed line represents the considered control volume. $\overline{u}_1$ is depth-averaged velocity at the paddle and $\overline{u}_2$ is depth-averaged velocity far away from the wave paddle. h is water depth, η is surge height, and $c_u(t)$ is unsteady celerity.

At the next instant, a second surge forms on top of the initial surge and these two surges form a new larger surge of height $\eta(t_2)$ and celerity $c_u(t_2)$. This surge formation process continues, and at each instant a part of the leading half of the solitary wave is formed. Described surge formation and formation of the leading half of the solitary wave is illustrated in Fig. 4.2. The proposed New methodology assumes the formation of surges *only* for the formation of the leading half of the solitary wave crest. It assumes a solitary wave of permanent shape that moves with the celerity of the last surge that forms the crest (calculated by substituting $\eta = H$ in Eqn. 4.10 below) for the formation of the trailing half of the solitary wave crest. Our reasoning behind generating the trailing half of the solitary wave crest with a constant celerity (i.e., maximum surge celerity) is the instabilities (such as widening of the wave profile that may lead to separation of the leading and trailing halves of the wave) that may arise as the wave propagates. However, it should be noted that, for our short wave-tank experiments, a notable instability is not observed for the case of generating waves using the unsteady celerity values calculated in Eqn. 4.10 for the entire wave profile.

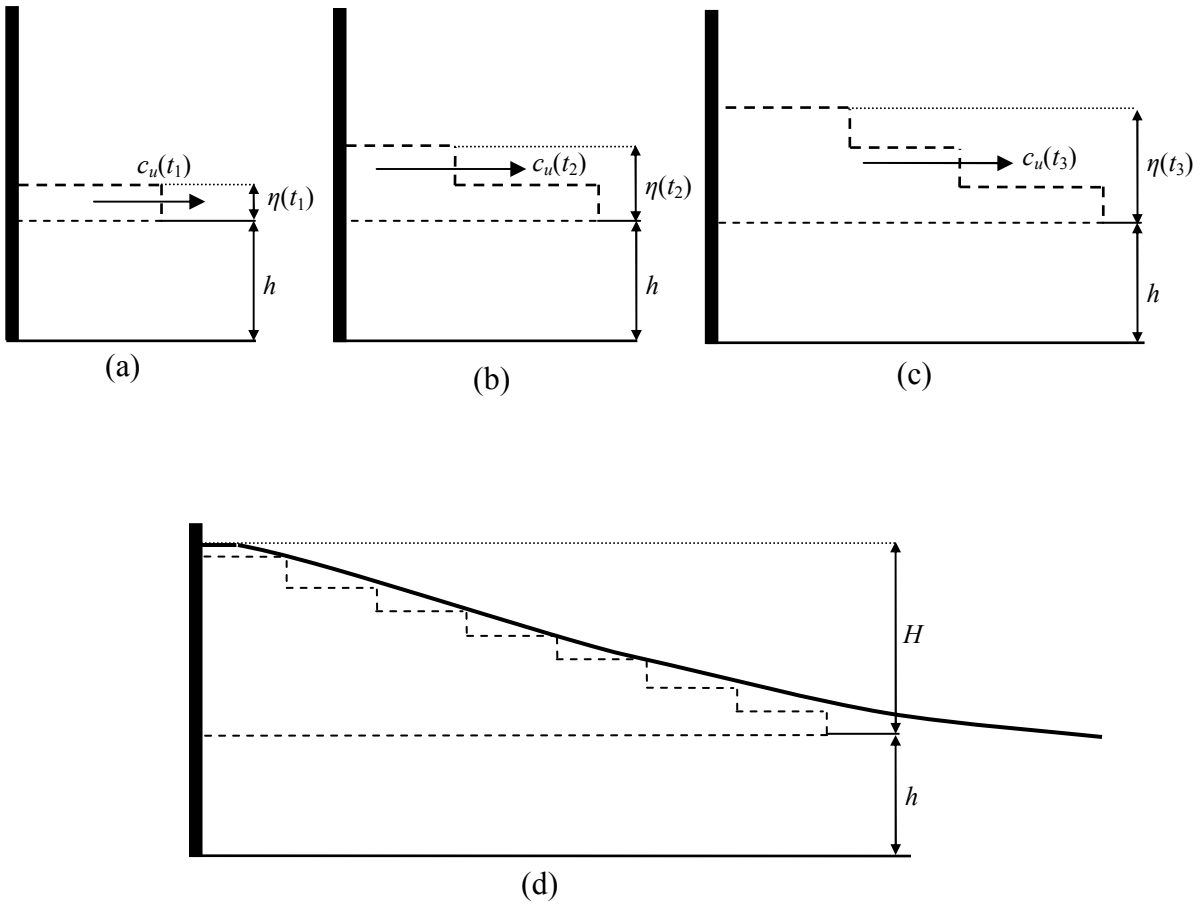

Figure 4.2 Theoretical illustration of the new idea behind the New methodology for the generation of solitary waves. Vertical dark block - wave paddle; horizontal solid line – wave-tank bottom; dashed line – surge boundary and still water level; curved solid line – generated solitary wave boundary, horizontal arrow – direction of surge propagation. Graphs in (a)-(c) are three sequential instances illustrating the formation of sequential surges and graph in (d) illustrates the formation of the leading half of the solitary wave by the sequential surges.

Derivation of the New methodology begins with the application of the conservation of mass principle. The integral form of the mass conservation equation for the CV presented in Fig. 4.1 can be written as follows [see also Chaudhry (2008)]:

$$\frac{d}{dt}\int_{cv}\rho\, d\forall + \sum_{cs}\rho UA = 0 \tag{4.1}$$

where ρ - density of water, $\forall$ - volume of the control volume, U – mean flow velocity at the corresponding CS, and A - flow area at the corresponding CS. The second term in Eqn. 4.1 can be expanded as:

$$\sum_{cs}\rho UA = \rho\,\overline{u}_1 A_1 - \rho\,\overline{u}_2\, A_2 = \rho\,\overline{u}_1\left(h+\eta\right)b - \rho\,\overline{u}_2\, hb \tag{4.2}$$

where b is the wave-tank width and subscripts 1 and 2 denotes quantities for control surfaces 1 and 2, respectively. Since water is incompressible, the first term in Eqn. 4.1 can be written as:

$$\frac{d}{dt}\int_{cv}\rho\, d\forall = \rho\frac{d}{dt}\int_{cv} d\forall = \rho\frac{c_u\,\eta\Delta t}{\Delta t}b = \rho\, c_u\,\eta b \tag{4.3}$$

where Δt is the incremental time interval. Substituting Eqns. 4.2 and 4.3 into Eqn. 2.1, it is possible to retrieve the mass conservation equation in the following form.

$$c_u\eta - \left(h+\eta\right)\overline{u}_1 = h\,\overline{u}_2 \tag{4.4}$$

Similarly, the integral form of the momentum conservation equation for the CV presented in Fig. 4.1 can be expressed as:

$$\sum F_{ext} = \sum_{cs} U\rho UA + \frac{d}{dt}\int_{cv}\rho U d\forall \tag{4.5}$$

where $\sum F_{\text{ext}}$ represents the summation of external forces acting on the system. Assuming that hydrostatic pressure distribution occurs on both sides of the CV (at CS1 and CS2), the summation of the external forces acting on the system is:

$$\sum F_{ext} = \gamma b \frac{(h+\eta)^2}{2} - \gamma b \frac{h^2}{2} \tag{4.6}$$

where γ is the specific weight of water. The first and second terms on the right side of Eqn. 4.5 can be expanded as:

$$\sum_{cs} \rho U^2 A = \rho u_2{}^2 bh - \rho u_1{}^2 b(\eta + h) \tag{4.7}$$

$$\frac{d}{dt} \int_{cv} \rho U d\forall = \rho b c_u \left(\overline{u}_1 (h+\eta) - \overline{u}_2 h \right) \tag{4.8}$$

Substituting Eqns. 4.6, 4.7, and 4.8 into Eqn. 4.5, one would obtain the momentum conservation equation in the following form.

$$\frac{g\eta}{2}(2h+\eta) = h\overline{u}_2{}^2 - (h+\eta)\overline{u}_1{}^2 + c_u \overline{u}_1 (h+\eta) - c_u \overline{u}_2 h \tag{4.9}$$

To simplify Eqns. 4.4 and 4.9, a long CV (such that CS2 is far away from the wave paddle) is conveniently chosen. Consequently, water particles at CS2 are assumed stationary (i.e., $\overline{u}_2 = 0$). This simplification reduces Eqn. 4.4 to the form of mass conservation equation in Eqn. 2.2 given by Svendsen (1974) for long waves of permanent form. Therefore, depth-averaged flow velocity at CS1, which is equal to the wave paddle velocity (hence, $\overline{u}_1$ is used to denote paddle velocity and depth-averaged flow velocity

interchangeably throughout the text), is obtained as a function of unsteady celerity and height of the surge:

$$\overline{u}_1 = \frac{c_u \eta}{(h+\eta)} \tag{2.2}$$

Substituting $\overline{u}_1$ from (2.2) and $\overline{u}_2 = 0$ into (4.9), unsteady celerity can be obtained as a function of surge height:

$$c_u(t) = \sqrt{g\left(h+\frac{\eta}{2}\right)\left(1+\frac{\eta}{h}\right)} \tag{4.10}$$

Note here that the surge height, η, appearing on the right hand side of Eqn. 4.10, which is the solitary wave elevation at the particular time [see Eqn. 2.3 for Boussinesq- and Rayleigh-type wave profiles], is a function of the steady celerity of the solitary wave, c, [$c = \sqrt{g(h+H)}$ for both Boussinesq- and Rayleigh-type waves]. From Eqns. 4.9 and 4.10, the paddle velocity, $\overline{u}_1$, can be calculated from the following parameterization:

$$\overline{u}_1 = \sqrt{g\frac{\eta}{h}\left(h+\frac{\eta}{2}\right)\left(\frac{\eta}{h+\eta}\right)} \tag{4.11}$$

Once the wave paddle velocity is determined at each instant, wave paddle trajectory, $\xi(t)$, is calculated by integrating Eqn. 4.12.

$$\frac{d\xi}{dt} = \overline{u}_1 = \sqrt{g\frac{\eta}{h}\left(h+\frac{\eta}{2}\right)\left(\frac{\eta}{h+\eta}\right)} \tag{4.12}$$

Since wave paddle position, ξ, appears on both sides of Eqn. 4.12 [solitary wave elevation, η, is a function of the wave paddle position; i.e., $\eta = H\,sech^2\,(k(ct - \xi)$ for Boussinesq- and Rayleigh-type wave profiles], Eqn. 4.12 is an implicit equation and should be solved numerically. Eqn. 4.12 can be discretized by a simple finite difference method to find ξ at each time step. In order to discretize the Eqn. 4.12, backward finite difference method was used. The position of wave paddle which is found in the previous time step was used in the right side to find the position of the wave paddle for the next time step. In the following descritization, subscripts i-1 and i refer to previous and present time steps respectively.

$$\frac{d\xi}{dt} = \sqrt{g\frac{\eta}{h}\left(h+\frac{\eta}{2}\right)\left(\frac{\eta}{h+\eta}\right)} \rightarrow \frac{\xi_i - \xi_{i-1}}{t_i - t_{i-1}} = \sqrt{g\frac{\eta_{i-1}}{h}\left(h+\frac{\eta_{i-1}}{2}\right)\left(\frac{\eta_{i-1}}{h+\eta_{i-1}}\right)} \tag{4.13}$$

$$\frac{\xi_i - \xi_{i-1}}{t_i - t_{i-1}} = \sqrt{g\frac{H\sec h^2\left(k\left(ct-\xi_{i-1}\right)\right)}{h}\left(h+\frac{H\sec h^2\left(k\left(ct-\xi_{i-1}\right)\right)}{2}\right)\left(\frac{H\sec h^2\left(k\left(ct-\xi_{i-1}\right)\right)}{h+H\sec h^2\left(k\left(ct-\xi_{i-1}\right)\right)}\right)}$$

Eqn. 4.13 can be solved for the position of the wave paddle, ξ_i. Following Goring (1979) and Guizien and Barthelemy (2002), duration of the paddle motion, T, and the paddle stroke length, S, are calculated using the analytical parameterizations [T=7.8/kc+S/c, and S=2H/kh] derived by Goring (1979). Since the outskirt decay coefficient, k, is unchanged in the New methodology, the total stroke of the wave paddle is the same as the one that is used in the Goring methodology. To avoid complexities and to be able to make direct comparisons with the waves generated using the Goring methodology, duration of the paddle motion, T, is calculated using the steady celerity values [$c = (g(h+H))^{1/2}$] as in the Goring methodology.

4.2 Experimental Procedure

Experiments were conducted in the rectangular wave-tank located at the Flow Physics Laboratory of Clemson University (see Chapter 3.1). The principle measurement of interest was the water surface elevation profiles. Water elevation data were collected using capacitance-type wave gauges. For each experimental condition, wave elevation data was recorded at fixed stations along the tank located at distances 2 *m* to 6 *m* downstream of the wave-paddle in equal steps of 1 *m* as illustrated in Fig. 3.1. Experiments were conducted for the still water depth, *h*, of 20 *cm* that is uniform along the tank up to the artificial beach at the end of the tank in order to dampen the waves (see Fig. 3.1). In the experiments, solitary waves with dimensionless wave height values, $\varepsilon = H/h$, ranging from 0.3 to 0.6 were generated. Two different solitary wave generation methodologies, Goring and our New methodology, were employed to generate the solitary waves based on two different first-order approximate solutions of solitary wave profile determined by Boussinesq (1872) and Rayleigh (1878). Photograph of a typical solitary wave generated in the wave-tank using the New methodology is presented in Fig. 4.3. A total of four sets of experiments [Boussinesq-type waves using the Goring methodology (GB), Rayleigh-type waves using the Goring methodology (GR), Boussinesq-type waves using the New methodology (NB), and Rayleigh-type waves using the New methodology (NR)] were conducted. Experimental conditions are summarized in Table 4.1.

Table 4.1 Experimental conditions for the solitary wave generation experiments

Exp. Run #	Methodology / Wave Profile	$\varepsilon = H/h$	S, m	T, s
1	GB	0.3	0.25	2.16
2	GB	0.4	0.29	1.85
3	GB	0.5	0.33	1.64
4	GB	0.6	0.36	1.48
5	GR	0.3	0.29	2.47
6	GR	0.4	0.35	2.19
7	GR	0.5	0.40	2.01
8	GR	0.6	0.45	1.87
9	NB	0.3	0.25	2.16
10	NB	0.4	0.29	1.85
11	NB	0.5	0.33	1.64
12	NB	0.6	0.36	1.48
13	NR	0.3	0.29	2.47
14	NR	0.4	0.35	2.19
15	NR	0.5	0.40	2.01
16	NR	0.6	0.45	1.87

Water depth, h, was 0.2 m in all experiments.
G : Goring Methodology N : New Methodology
T :Duration of wave paddle motion S : Stroke length for the wave paddle motion

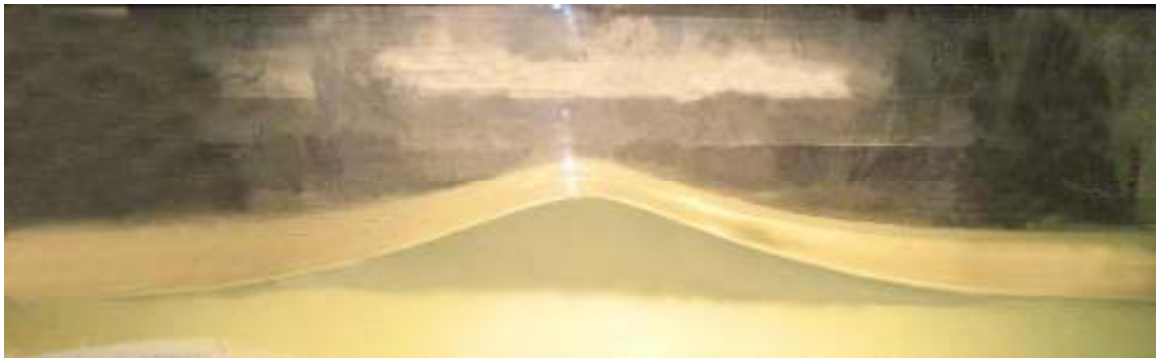

Figure 4.3 Photograph of a typical solitary wave generated in the wave-tank. Rayleigh-type solitary wave generated by the New methodology for $\varepsilon = 0.6$ in still water depth of $h = 20$ cm. Photographed at $15h$ from the wave paddle.

4.3 Results and Discussions

In this section, characteristics of generated solitary waves using the proposed New methodology are presented. Comparisons with the waves generated using the traditional methodology by Goring are included to demonstrate the capabilities of the New methodology. Main solitary wave characteristics of interest are profile shape, amplitude, change in the profile shape, wave amplitude attenuation, and propagation speed. In the results presented below, the characteristics of the aimed Boussinesq- and Rayleigh-type solitary waves served as the benchmark, and the conclusions on the capabilities of the New methodology as well as the Goring methodology are drawn based on the degree of resemblance of the generated wave characteristics to the characteristics of the aimed Boussinesq- and Rayleigh-type solitary waves. Results of these comparisons are as follows.

Comparisons of the generated solitary wave profiles measured at distances x=10h (left panel) and 20h (right panel) from the initial position of the wave-paddle are presented in Figs. 4.4 and 4.5. In these figures, graphs are plotted for the dimensionless water surface elevation, η/H, (vertical coordinate axes) versus the dimensionless time, $t\sqrt{g/h}$, (horizontal coordinate axes). In these graphs, thick solid lines represent the profiles of generated waves by the New methodology, thin solid lines represent the profiles of generated waves by the Goring methodology, and the dashed lines represent the profiles of the aimed Rayleigh- (Fig. 4.3) and Boussinesq-type (Fig. 4.4) solitary waves. As can be seen from these figures, profiles of the waves generated by the New methodology clearly resemble the aimed Boussinesq- and Rayleigh-type solitary wave profiles closer

than the waves generated by the Goring methodology. Moreover, these figures along with the figures that are discussed below indicate that waves generated using the New methodology can be considered as established solitary waves even at $x=10h$. Wave profiles generated by both methods resemble the aimed Rayleigh-type solitary wave profiles closer than the aimed Boussinesq-type solitary wave profiles. This observation is also reported by Guizien and Barthelemy (2002) in the case of Goring methodology.

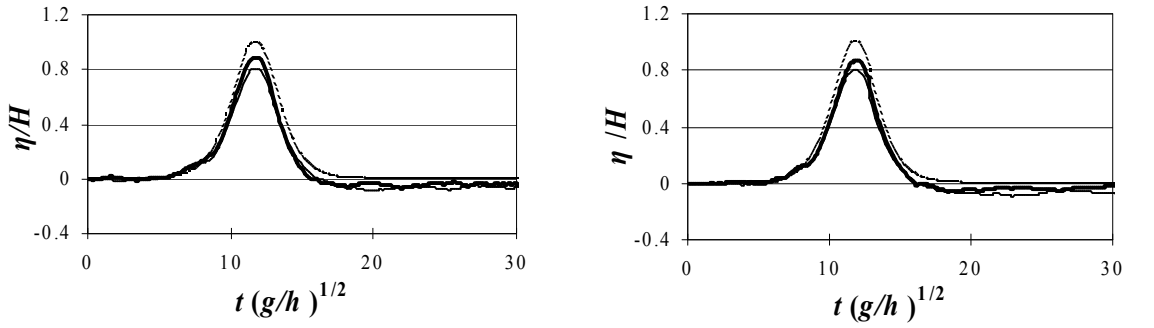

(*a*) $\varepsilon = 0.3$

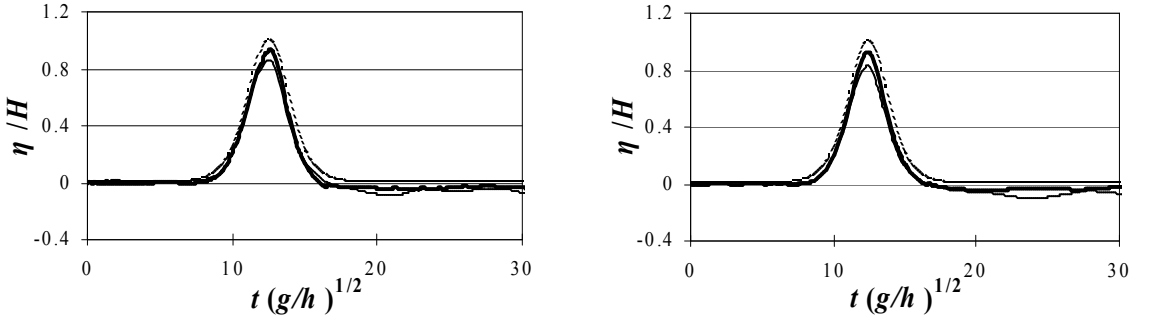

(*b*) $\varepsilon = 0.4$

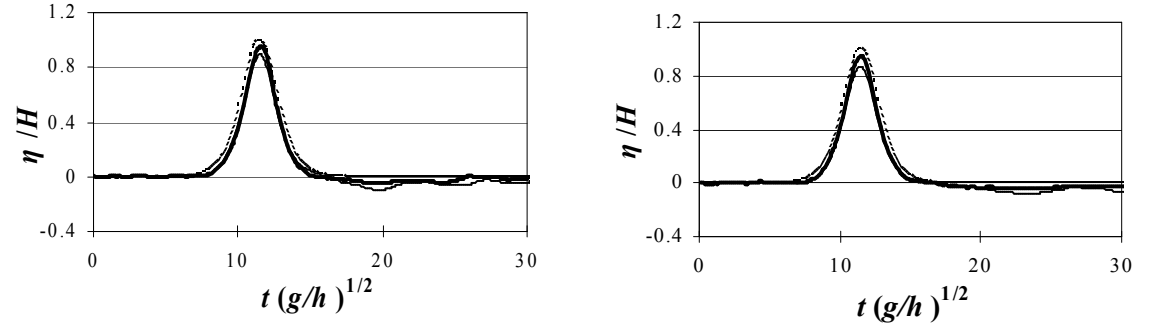

(*c*) $\varepsilon = 0.5$

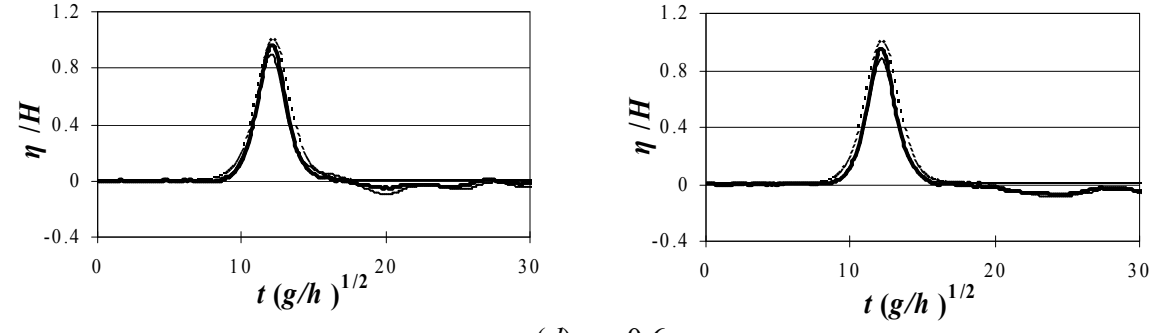

(*d*) $\varepsilon = 0.6$

Figure 4.4 Wave elevation data recorded for generated Rayleigh-type solitary waves. Water surface profiles recorded at $x = 10h$ (left) and $20h$ (right) away from the wave paddle with $h = 0.2$ *m*. New Method (——); Goring Method (—); Rayleigh solution profile (-----).

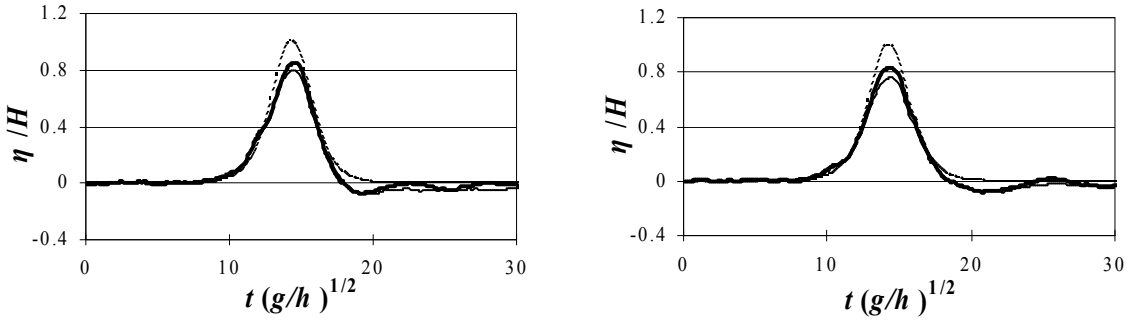

(*a*) $\varepsilon = 0.3$

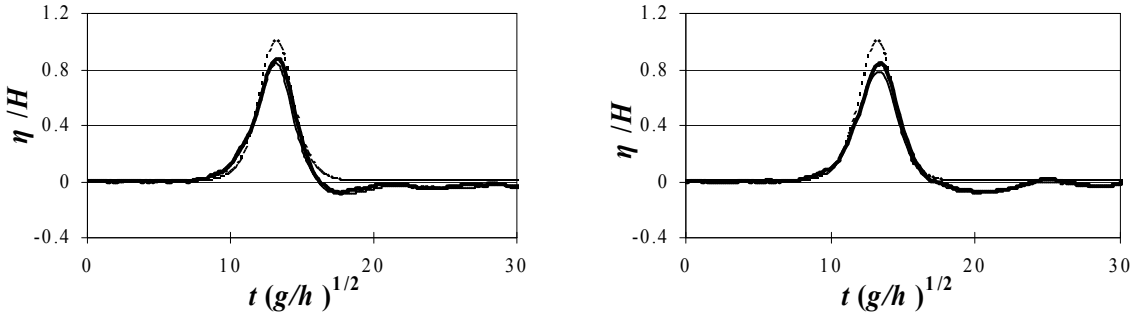

(*b*) $\varepsilon = 0.4$

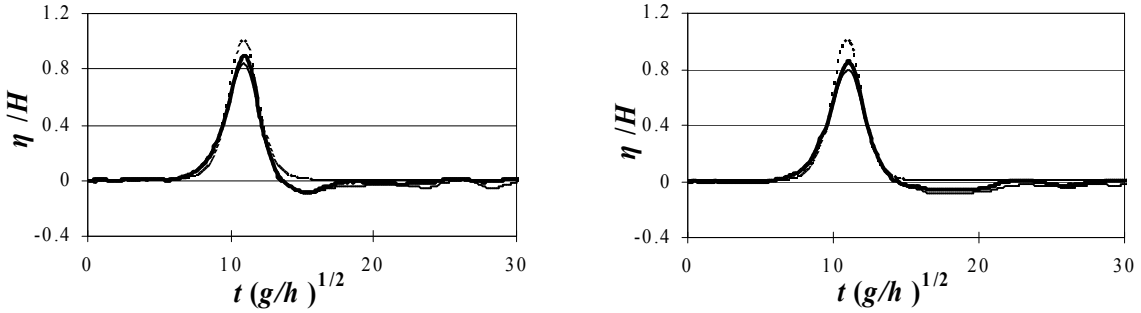

(*c*) $\varepsilon = 0.5$

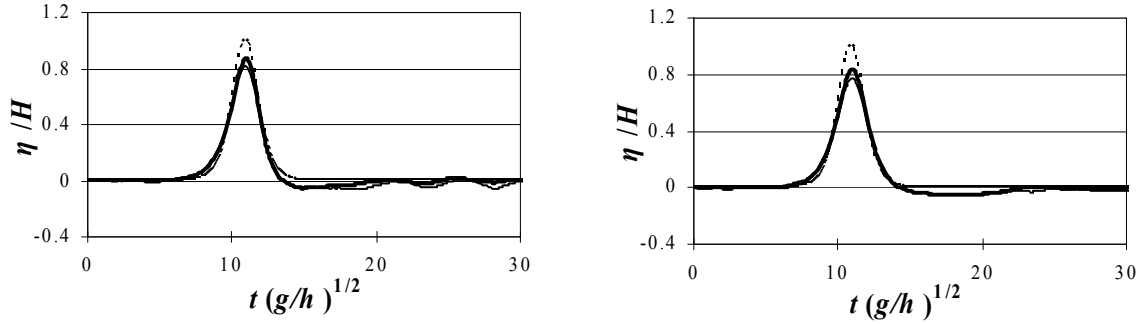

(*d*) $\varepsilon = 0.6$

Figure4.5 Wave elevation data recorded for generated Boussinesq-type solitary waves. Water surface profiles recorded at $x = 10h$ (left) and $20h$ (right) away from the wave paddle with $h = 0.2\ m$. New methodology (——); Goring Methodology (—); Rayleigh solution profile (-----).

In Figs. 4.4 and 4.5, the hump of the generated wave is followed by a long depression below the still water level that consists of a series of dispersive oscillatory trailing waves. Solitary waves generated using the New methodology are followed by smaller depressions, compared to those generated by the Goring methodology. Moreover, Rayleigh-type solitary waves generated by either method are associated with smaller depressions compared to Boussinesq-type solitary waves generated using the same methodology. For generated Rayleigh-type waves at x=10h, amplitude of the depressions are observed to be less than 4.5% of the crest heights for the waves generated using the New methodology and to be less than 8% of the crest heights for the waves generated using the Goring methodology. On the other hand, for generated Boussinesq-type waves at x=10h, amplitudes of the depressions are observed to be less than 7% of the crest heights for the waves generated using the New methodology and to be less than 9% of the crest heights for the waves generated using the Goring methodology. Relative amplitudes of the depressions (ratio of the depression amplitude and the crest/wave height) observed at x = 10h and 30h in each experimental run are tabulated in Table 4.2. Amplitudes of the depressions decrease gradually as the solitary waves propagate along the wave-tank. Furthermore, since the celerities of the depressions are smaller than the celerities of the humps, depressions separate from the humps gradually as the waves propagate along the tank. This separation process can be considered as a progression towards the established solitary wave form that consists of only a hump. However, the longer the distance it takes for the separation to occur, the more dispersive effects act on the hump, changing its outskirt profile and reducing its celerity. The separation process occurs over a shorter distance for the generated waves with larger ε values, since the

celerities of the generated humps are larger (see Figs. 4.3 and 4.4). Moreover, depressions are detached from the hump in shorter distances for the generated Rayleigh-type waves as compared to the generated Boussinesq-type waves for the same experimental conditions. The reasons are believed to be: (i) the larger celerity of the generated Rayleigh-type waves, and therefore, the larger difference between the celerity of the main hump and trailing waves compared to the generated Boussinesq-type waves (ii) nonlinear effects are more pronounced in the generated Boussinesq-type waves, whereas the linear effects of frequency dispersion are more comparable with the nonlinear effects in the generated Rayleigh-type waves. Therefore, the frequency dispersion separates the trailing waves of higher frequency faster and more effective from the main hump of lower frequency in the Rayleigh-type waves.

Table 4.2 Relative depression amplitudes and profile changes for the generated waves

Exp. #	Methodology / Wave Profile	$\varepsilon = H/h$	a_t/H_{exp} at $10h$	a_t/H_{exp} at $30h$	Profile change from $10h$ to $30h$ $\Omega_{exp} / \Omega_{theo}$
1	GB	0.3	0.070	0.060	10.24%
2	GB	0.4	0.078	0.070	8.35%
3	GB	0.5	0.084	0.08	7.69%
4	GB	0.6	0.060	0.057	7.23%
5	GR	0.3	0.087	0.070	8.49%
6	GR	0.4	0.083	0.065	8.47%
7	GR	0.5	0.08	0.064	8.28%
8	GR	0.6	0.09	0.08	7.63%
9	NB	0.3	0.068	0.060	7.53%
10	NB	0.4	0.076	0.071	5.48%
11	NB	0.5	0.083	0.079	5.05%
12	NB	0.6	0.055	0.052	4.68%
13	NR	0.3	0.062	0.045	6.67%
14	NR	0.4	0.044	0.038	4.44%
15	NR	0.5	0.040	0.035	3.41%
16	NR	0.6	0.045	0.041	3.37%

Water depth, h, was 0.2 m in all experiments.

As Figs. 4.4 and 4.5 illustrate, the separation of depressions from the humps occurs in a shorter distance for the waves generated using the New methodology compared to the waves generated using the Goring methodology. For both Boussinesq- and Rayleigh-type waves generated using the New methodology, the separation of the depressions from the humps are clear after propagating a distance of $30h$ or less. However, a clear detachment of the depressions from the hump for Boussinesq-type waves generated using the Goring methodology are not observed throughout the entire length of the tank, while detachment within the length of the tank is observed for the Rayleigh-type waves only with ε values of 0.5 and 0.6. Waves of higher amplitude propagate faster; in higher ε values, the difference between the celerity of the main waveform and the trailing waves is larger and therefore, trailing waves detach faster from the main hump.

In order to compare the characteristics of the generated wave profiles (i.e., wave height, H_{exp}, and solitary wave frequency, Ω_{exp}, which represents the profile shape) using both of the generation methodologies with the characteristics of the proposed Boussinesq- and Rayleigh-type wave profiles, experimental wave elevation data are fitted by Eqn. 4.14 below. This equation has the same functional form as the profiles of the Boussinesq- and Rayleigh-type waves given in Eqn. 2.3. A curve fitting analysis is necessary because wave gauge measurements are discrete (sampling frequency of 50 *Hz*) and celerities of the generated waves (1 – 2 *m*/*s*) are large; therefore, maximum wave elevation values measured do not necessarily correspond to the generated wave height values and the recorded wave elevation profiles are not necessarily symmetrical with respect to the recorded highest wave elevations as can be seen in Figs. 4.4 and 4.5. Moreover, this analysis is necessary to estimate the solitary wave frequencies of the generated waves. There are three unknowns in Eqn. 4.14 (solitary wave frequency, Ω_{reg}; wave height, H_{reg}; and time fitting parameter, t_0), which are determined using the least squares method.

$$\eta_{exp} = H_{reg} \operatorname{sech}^2 (\Omega_{reg} (t - t_0)) \tag{4.14}$$

Ω_{reg} determined from the fitting analysis is considered as the experimental solitary wave frequency, and hereafter is referred as Ω_{exp}. Eqn. 4.14 is fitted to the top 95% (i.e., wave elevation values larger than 5% of the wave height) of the recorded wave profile. The reason for choosing the top 95% is that the depression with the trailing waves following the hump alters the smooth experimental solitary wave profile approximately within the bottom 5% of the wave profile. In order to avoid the unrealistic values for H_{reg}, its value is forced to be within ± 2% of the maximum recorded water elevation. Result of a typical

fitting analysis is presented in Fig. 4.6 by comparing the experimental data with its best fit.

In Fig. 4.7, H_{exp}/H_{theo} [H_{theo} - theoretical wave height value for the aimed Rayleigh (a) or Boussinesq (b) type waves] at x=10h (2 m) for the waves generated using the Goring and the New methodologies are presented. As can be clearly seen from this figure, compared to the wave height values of the generated waves using the Goring methodology, wave height values of the generated waves using the New methodology are closer to the wave height values of the aimed Rayleigh- and Boussinesq-type waves.

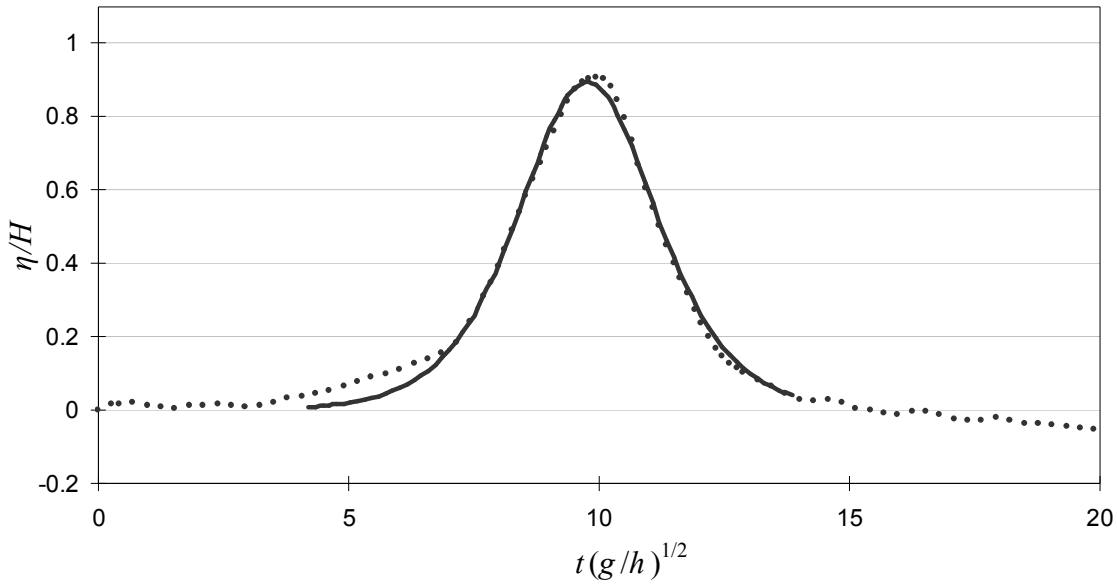

Figure 4.6 A typical fitting analysis output. Recorded water surface elevation (**…**) and fitted curve (**—**).

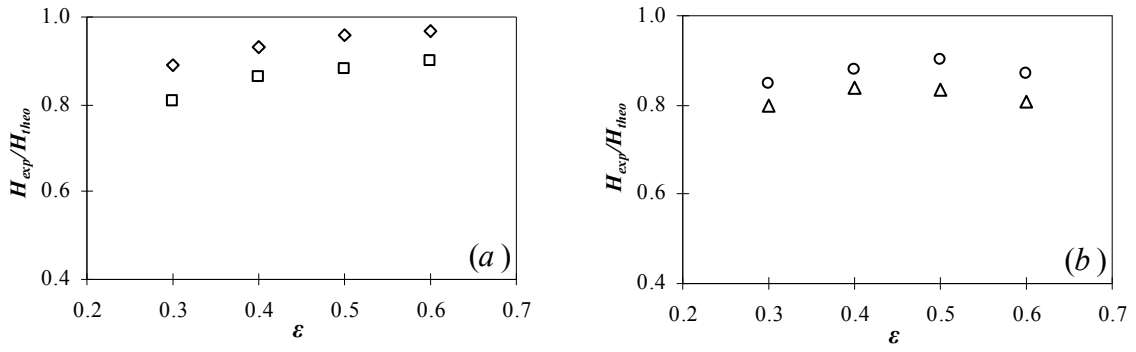

Figure 4.7 Experimental wave heights at $x = 10h$ from the wave paddle. a) Rayleigh-type waves [the New methodology (◊); Goring methodology (□)]. b) Boussinesq-type waves [the New methodology (o); Goring methodology (Δ)].

Solitary wave is a permanent waveform that may propagate long distances without a change in their characteristics. Therefore, we considered the dispersive characteristics of the generated waves in the laboratory as an indication in assessing the resemblance of the generated waves to the aimed solitary waves. Moreover, it is clear that the dispersive characteristics of the generated waves should be taken into consideration for large-scale laboratory studies in which waves propagate tens of meters before reaching to the measurement station. To examine the dispersive characteristics of the generated waves, the attenuation trends for the heights and frequencies of the generated waves as they propagate along the tank are investigated.

For a solitary wave propagating in the wave-tank, in addition to the wave damping inherent to the dispersive characteristics of the generated waves, frictional wave damping occurs due to the sidewalls and bottom wall. In order to assess the wave attenuation (hence, dispersive characteristics) characteristics of the generated waves solely due to the generation mechanism in the absence of frictional damping, a comparison between the

observed wave height attenuation of the generated solitary waves and the predicted wave height attenuation of the waves only due to frictional damping is given in Figs. 4.8 and 4.9. Predictions for wave height attenuations due to frictional damping as the waves propagate along the tank are calculated based on the following analytical parameterization proposed by Keulegan (1948).

$$\left(\frac{H_2}{h}\right)^{-1/4} = \left(\frac{H_1}{h}\right)^{-1/4} + \frac{1}{12}\left(1+\frac{2h}{b}\right)\frac{l}{h}\sqrt{\frac{\upsilon}{g^{1/2}h^{3/2}}} \tag{4.15}$$

Here, H_2 is the attenuated height of the wave at a distance of l from a reference position that the wave has already passed through with a height of H_1, b is the width of the tank, and υ is the kinematic viscosity of water. In frictional wave damping calculations presented in Figs. 4.8 and 4.9, reference wave height, H_1, is selected to be the experimental wave height value recorded by the first wave gauge at $x = 10h$ (2 m); hence, denoted as $H_{\text{exp-}10h}$. In Figs. 4.8 and 4.9, the relative experimental wave heights, $H_{exp}/H_{exp\text{-}10h}$, at different distances along the wave-tank are presented for Rayleigh- (Fig. 4.8) and Boussinesq-type (Fig. 4.9) waves generated using both the Goring and the New methodologies. In the graphs given in these figures, the deviation of the relative experimental wave height values (solid lines) from the wave attenuation predictions due to frictional damping (dashed lines) may be interpreted to infer the establishment characteristics of the generated waves, i.e., the less deviation from the predictions the more established generated waves. As can be clearly seen from these graphs, the waves generated using the New methodology follow the Keulegan's predictions for the frictional damping better and undergo less attenuation compared to those generated by the Goring methodology; hence, indicating that less dispersive waves are generated using

the New methodology. This observation may be explained by the fact that the wave profiles generated using the New methodology have smaller depression amplitudes as well as demonstrate faster separation of the depressions and the humps compared to the waves generated using the Goring methodology. Comparing the graphs in Figs. 4.8 and 4.9, it can be seen that the heights of Rayleigh-type waves attenuate less than the heights of Boussinesq-type waves. This observation supports the observation of Guizien and Barthelemy (2002) that the attenuation of Rayleigh-type waves follows Keulegan's predictions better than Boussinesq-type waves which undergo severe damping that cannot be explained only by friction. Guizien and Barthelemy (2002) attributed this difference in the observed wave attenuation characteristics to different definitions of outskirt decay coefficient, k, in Boussinesq- and Rayleigh-type waves. Another reason for the observed difference is the difference in the characteristics of the depressions formed in the laboratory generation of Boussinesq- and Rayleigh-type waves. As mentioned earlier, depressions have larger amplitudes and are attached to the humps for a longer distance for Boussinesq-type waves compared to Rayleigh-type waves. Therefore, depressions are expected to have more pronounced dispersive effects on Boussinesq-type waves. Since the wave profiles generated using the New methodology resemble the aimed theoretical solitary wave profiles better and have smaller depression amplitudes as well as demonstrate faster separation of the depressions and the humps compared to the waves generated using the Goring methodology, the latter reasoning may also explain the improved establishment rate of the waves generated using the New methodology.

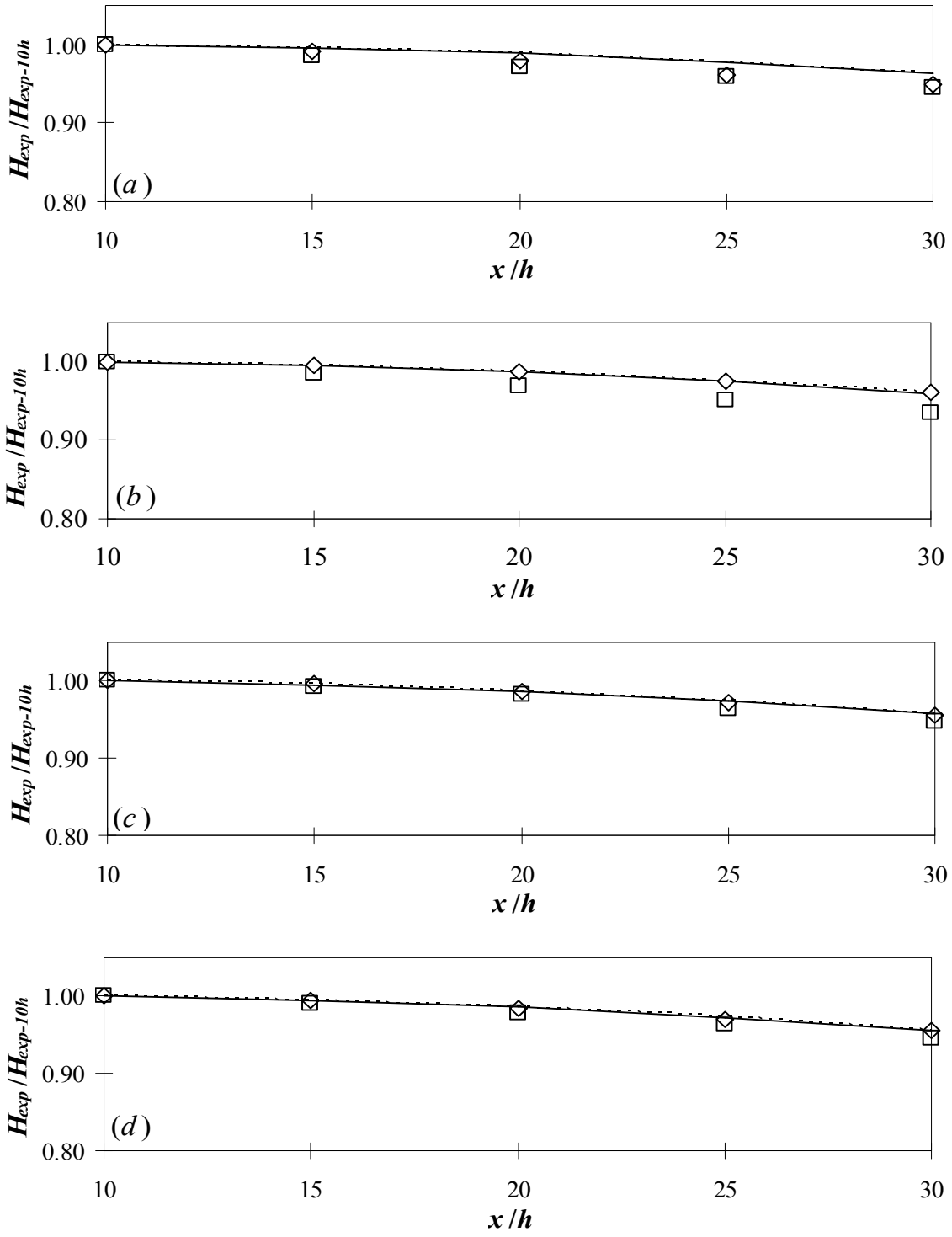

Figure 4.8 Attenuation of generated Rayleigh-type waves with distance. Waves generated using the New methodology (◊) and the corresponding Keulegan's prediction (Eqn. 4.15) (—); waves generated using the Goring's methodology (□) and the corresponding Keulegan's prediction (Eqn. 4.15) (- - -). (*a*) – (*d*) corresponds to ε = 0.3, 0.4, 0.5, and 0.6 respectively.

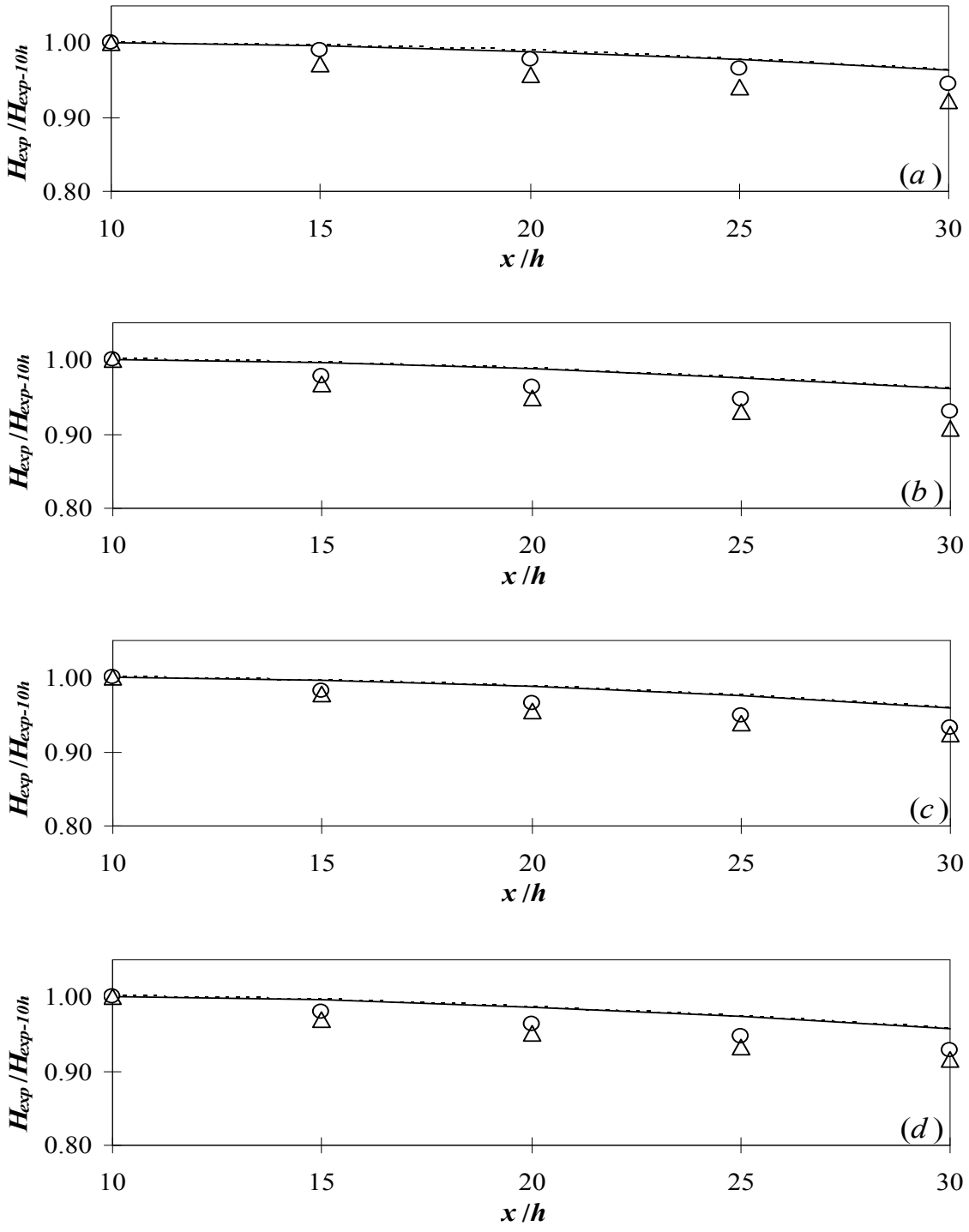

Figure 4.9 Attenuation of generated Boussinesq-type waves with distance. Waves generated using the New methodology (o) and the corresponding Keulegan's prediction (Eqn. 4.15) (—); waves generated using the Goring methodology (Δ) and the corresponding Keulegan prediction (Eqn. 4.15) (- - -). (*a*) – (*d*) corresponds to ε = 0.3, 0.4, 0.5, and 0.6 respectively.

The second process of interest in assessing the dispersive characteristics of the generated waves is the change in wave profile shape as the waves propagate along the tank. The parameter that characterizes the solitary wave profile shape is the solitary wave frequency, $\Omega = kc$. In Figs. 4.10 and 4.11, the ratios of the experimental solitary wave frequencies, Ω_{exp}, and their theoretical values, Ω_{theo} [$\Omega_{theo} = \sqrt{3Hg/\left(4h^2\right)}$ for Rayleigh-type waves in Fig. (4.10), and $\Omega_{theo} = \sqrt{3Hg(h+H)/\left(4h^3\right)}$ for Boussinesq-type waves in Fig. (4.11)] at different positions along the tank are given. Note that the values of these ratios closer to unity indicate the closer resemblance of the generated wave profiles to the aimed theoretical solitary wave profiles and the smaller changes in these ratio values along the tank (i.e., milder slopes of the curves in Figs. 4.10 and 4.11 indicate less dispersion of the generated waves. Therefore, from Figs. 4.10 and 4.11, it can be concluded that the profiles of the waves generated using the New methodology resemble the aimed wave profiles closer and disperse less as they propagate along the tank compared to the ones generated by the Goring methodology for all the experimental conditions studied. The change in the ratios of the experimental and theoretical solitary wave frequencies from x=10h to x=30h is observed to be confined within 4.5% to 7.5% of the initial ratios (at x=10h) for the Boussinesq-type waves and 3.5% to 6.5% of the initial ratios for the Rayleigh-type waves generated using the New methodology whereas frequency change for the waves generated by the Goring methodology is observed to be confined within 7.5% to 10.5% of the initial ratios for Boussinesq-type waves and 7.5% to 8.5% of the initial ratios for Rayleigh-type waves. Percentage change values for the ratio of experimental and theoretical frequencies of the

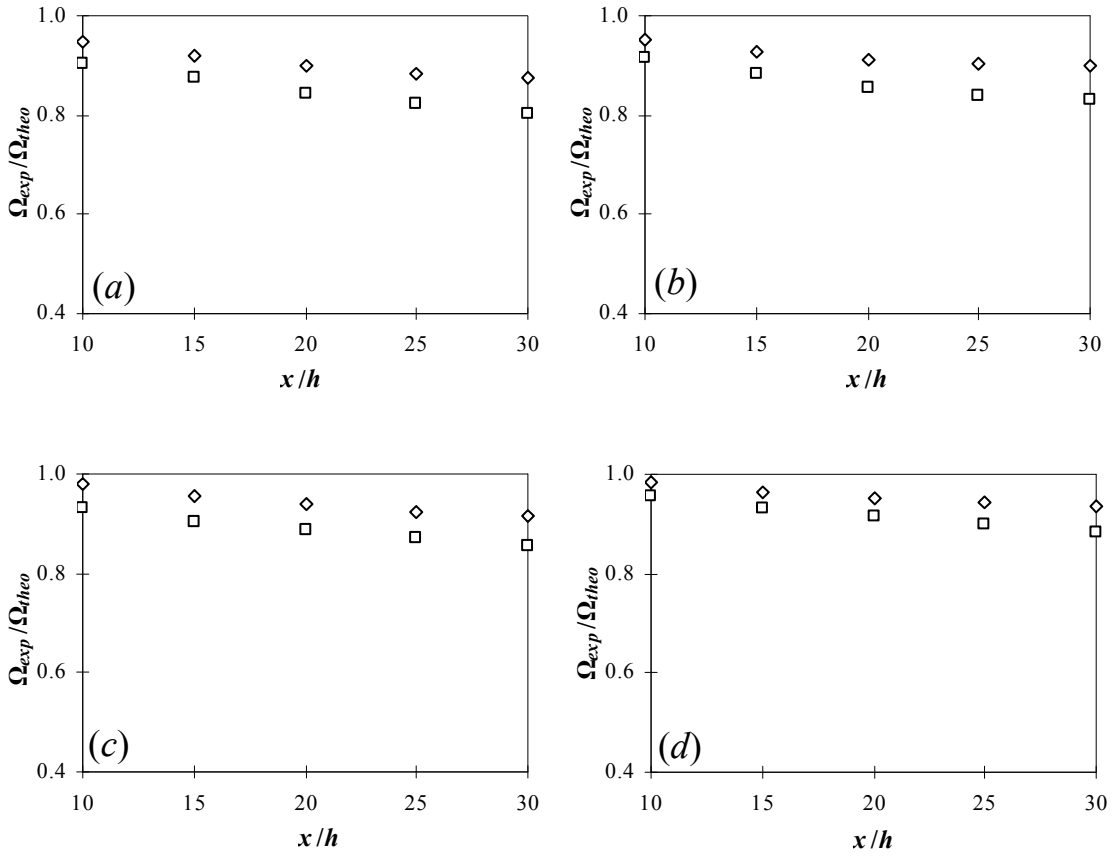

Figure 4.10 Solitary wave frequency ratios (experimental to theoretical) along the wave-tank for Rayleigh-type waves generated using the New methodology (◊) and the Goring methodology (□). (*a*) – (*d*) corresponds to ε = 0.3, 0.4, 0.5, and 0.6 respectively.

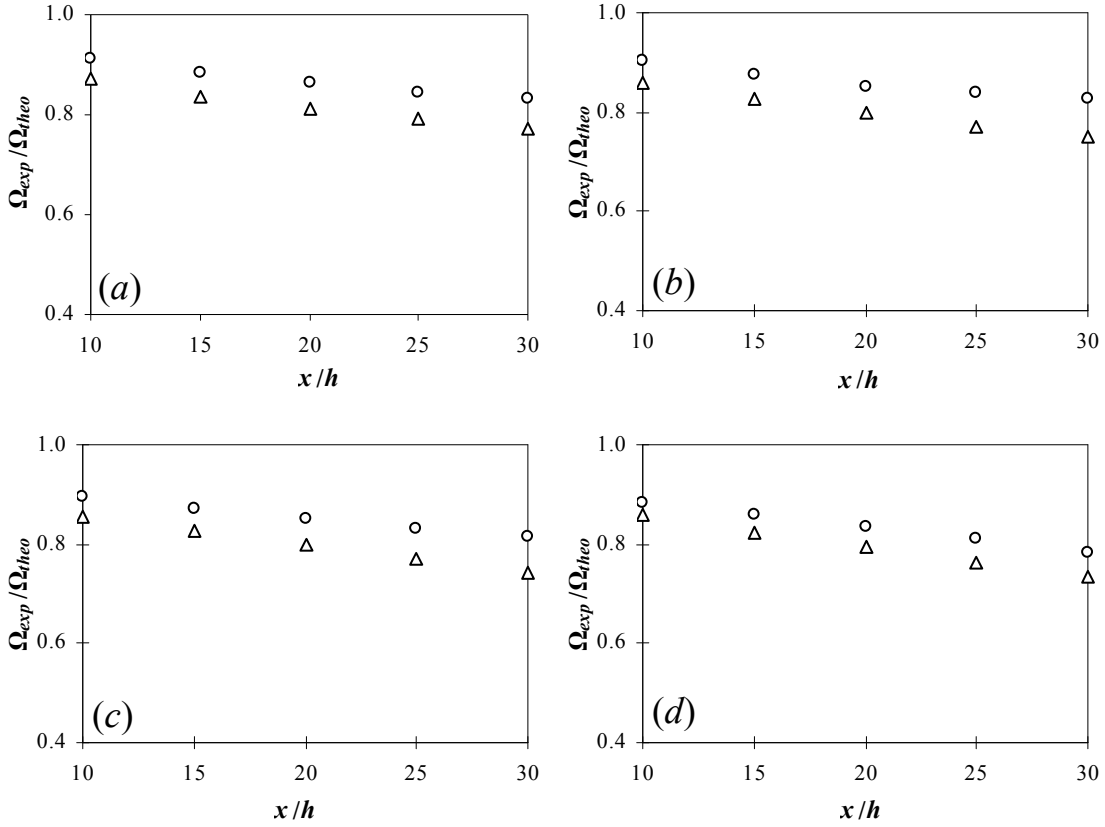

Figure 4.11 Solitary wave frequency ratios (experimental to theoretical) along the wave-tank for Boussinesq-type waves generated using the New methodology (o) and the Goring methodology (Δ). (*a*) – (*d*) corresponds to ε = 0.3, 0.4, 0.5, and 0.6 respectively.

solitary waves propagating from x = 10h to 30h for each experimental run are tabulated in Table 4.2.

Observed wave attenuation and profile change characteristics of the generated waves along the wave-tank indicate that the nonlinear effects balance the dispersive effects better for the waves generated by the New methodology compared to the waves generated by the Goring methodology. Rayleigh-type waves generated using either of

the generation methodologies are observed to resemble the aimed waves better than the Boussinesq-type waves.

Finally, the average experimental propagation velocities of the generated waves, c_{exp}, are compared with the theoretical propagation velocities of the aimed solitary waves, c_{theo}, as shown in Fig. 4.12 [$c_{theo} = \sqrt{g(h+H)}$ for both Boussinesq- and Rayleigh-type waves]. Average experimental celerities are determined from the wave gauge recordings at x=10h and x=30h by dividing the distance traveled by the hump (i.e., 20h) by the time elapsed during this travel. Due to accuracy considerations, an average experimental celerity is calculated over the measurement section and change in the experimental celerities are not considered. In Fig. 4.12, it can be seen that ratios of the average experimental and theoretical celerities of the waves generated by the New methodology are within 1.3% neighborhood of unity for the Rayleigh-type waves and 3.2% of unity for the Boussinesq-type waves. On the other hand, these celerity ratios for the waves generated by the Goring method are within 4.8% neighborhood of unity for the Rayleigh-type waves and 8.2% of unity for the Boussinesq-type waves. Like the salient characteristics discussed above, this observation indicates that celerities of the waves generated by the New methodology are in better agreement with the aimed wave celerities as compared to the celerities of the waves generated by the Goring methodology. Moreover, celerities of the generated Rayleigh-type waves demonstrated a better agreement with the celerities of the aimed waves in comparison to Boussinesq-type waves.

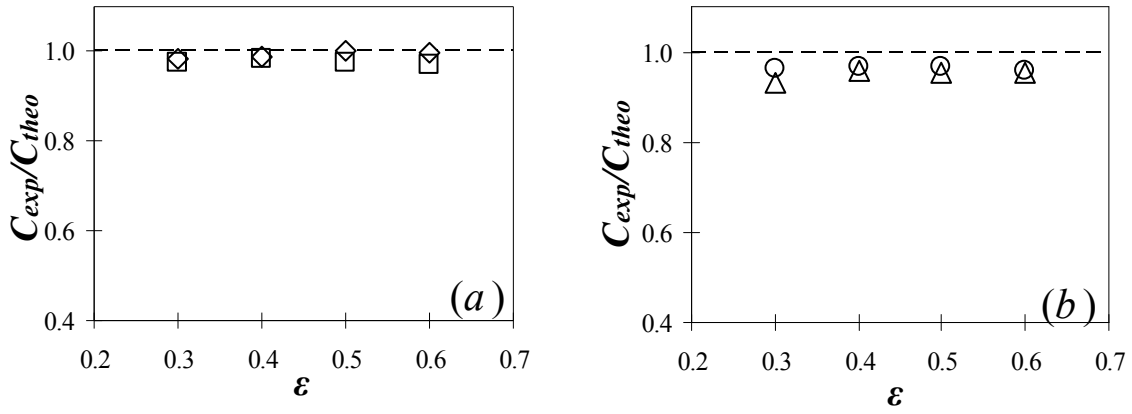

Figure 4.12 Experimental to theoretical solitary wave celerity ratio vs. dimensionless wave height (a) for Rayleigh-type waves generated using the New methodology (◊) and the Goring methodology (□); (b) for Boussinesq-type waves generated using the New methodology (o) and the Goring methodology (Δ).

CHAPTER FIVE

WATER SURFACE DEPRESSIONS

This chapter, discussing on the water surface depressions, consist of two parts. In the first part of this chapter, the trajectory of the wave paddle for the generation of water surface depressions using the Goring methodology is derived and a series of experiments were conducted in a water depth of 30 *cm* to examine the Goring methodology in generating water surface depressions. In the second part of this chapter, a large set of experiments were conducted in three different water depths of 6 *cm*, 10 *cm*, and 15 *cm* with which the propagation characteristics of water surface depressions in terms of profile shape, amplitude attenuation, and celerity were investigated. Observations are discussed in detail by presenting the recorded data. After identifying the important dimensionless parameters involved in the propagation of depressions, empirical parameterizations for characterizing the propagation characteristics of the water surface depressions are proposed.

5.1 Wave Generation Methodology

The traditional methodology by Goring (1979) for the generation of elevation solitary waves by piston-type wavemakers is employed to generate water surface depressions. The details of this wave generation methodology is given in Chapter 2. Briefly, this traditional methodology assumes that, during the generation, the horizontal component of the water particle velocity next to the wave-paddle is equal to the velocity of the wave-paddle:

$$\frac{d\xi}{dt} = \bar{u}(\xi, t) \tag{2.1}$$

This horizontal component of the water particle velocity along the wave-tank is assumed to be constant throughout the water depth. Based on the conservation of mass considerations, Svendsen (1974) derived the the depth-averaged velocity for long waves of permanent form as follows:

$$\bar{u}(\xi, t) = \frac{c\,\eta(\xi, t)}{h + \eta(\xi, t)} \tag{2.2}$$

Water surface depressions do not have any particular theoretical profile. In the present study, a negative solitary wave is chosen as a profile of water surface depressions to derive the trajectory of the wave paddle. The 1st order approximate solution of the Euler equation for solitary waves by Boussinesq (1871) is used in Eqns. 2.2 as:

$$\eta = -a_t \operatorname{sech}^2[k(ct - \xi)] \tag{5-1}$$

where a_t is the amplitude of the aimed negative solitary wave, k is the boundary/outskirt decay coefficient, [$k = \sqrt{3H/(4h^3)}$ from Boussinesq (1871)], and c is the celerity of the depression. The propagation speed of a depression solitary wave is very close to the celerity of long gravity waves defined as $\sqrt{gh}$. Korteweg and De-Vries (1895) derived the theoretical celerity of depression solitary waves as $\sqrt{gh}(1 - a_t/2h)$. Boussinesq (1871) and Rayleigh (1878) for the 1st order approximate solutions of Euler equation found the celerity of depression solitary waves as $\sqrt{g(h - a_t)}$. The celerity values obtained from these equations are very close. In the wave-paddle trajectory calculations for the generation of water depressions, the celerity is calculated by the equation derived

by Korteweg De-Vries (1895) for the water surface depression profile of Eqn. 5.1. A typical profile of the aimed depression solitary wave is shown in Fig. (5.1*b*).

By solving Eqns. 2.1, 2.2, and 5.1 simultaneously, an implicit relationship for the trajectory of the wave-paddle, $\xi(t)$, is obtained (see Goring, 1979 for the details of the derivation):

$$\xi(t) = -\frac{a_t}{kh}\tanh\left(k\left(ct - \xi\right)\right) \tag{5.2}$$

From Eqn. 5.2, the total stroke length of the wave-paddle, S, calculated as $2a_t/kh$. Ideally, for the generation of a depression solitary wave, Eqn. 5.2 implies an infinite duration of the wave paddle motion. However, in order to make it applicable for the laboratory wave generations, the trajectory of the wave paddle should be cut off. Rearranging Eqn. 5.2 in terms of t, gives:

$$t = \frac{\tanh^{-1}\left(\dfrac{\xi kh}{a_t}\right)}{kc} + \frac{\xi}{c} \tag{5.3}$$

For practical purposes, as noted by Goring (1979), any value close enough to unity can be chosen to replace $\xi kh/a_t$. Goring (1979) used 0.999 and assumed that this is close enough to maintain the desired accuracy of the wave paddle trajectory. By introducing $\xi kh/a_t$ = 0.999 into Eqn. 5.3, the relationship for the total duration of the wave paddle, T, is derived as:

$$T = \frac{7.6}{kc} + \frac{S}{c} \tag{5.4}$$

In Eqn. 5.4, c is the theoretical celerity of the depression solitary waves determined by the equation proposed by Korteweg and De-Vries (1895) as $c = \sqrt{gh}\left(1 - a_t/h\right)$. A typical

trajectory of the wave paddle and the corresponding aimed depression solitary wave is shown in Fig. 5.1.

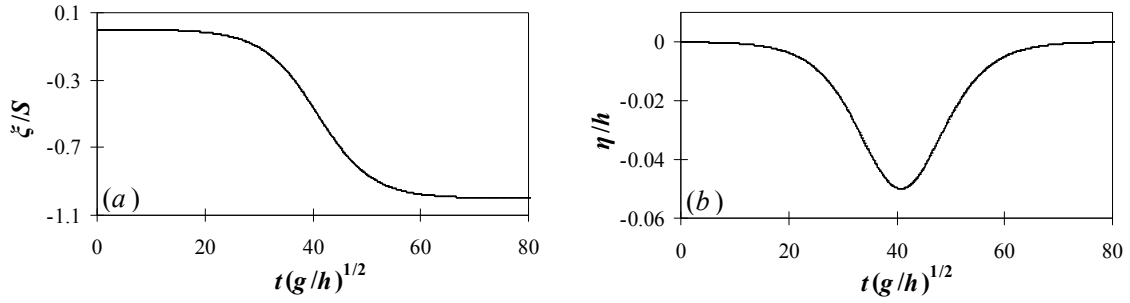

Figure 5.1 (*a*) A typical trajectory of the wave-paddle for generating a depression solitary wave. (*b*) Theoretical profile of the aimed depression solitary wave. Graphs are for $\varepsilon_t = a_t/h = 0.05$ in a still water depth of 30 *cm*.

In order to examine the depression wave generation methodology outline above, water surface depressions were generated in a still water depth of 30 *cm* that was uniform along the tank up to the steep sandy beach (see Fig 3.1). Water surface elevation data were recorded from 1.5 *m* ($x = 5h$) upto 6 *m* ($x = 20h$) from the wave paddle in equal steps of 1 *m* except for the second wave gauge which is placed at a distance of 50 *cm* from the first one. Depression solitary waves with relative trough amplitude values ranging from 0.05 to 0.15 were generated.

Table 5.1 Experimental conditions and details for the generation of water surface depressions

Exp. Run #	h (cm)	$\varepsilon_t = a_t/h$	c (m/s)	k (m^{-1})	S (m)	T (s)
1	30	0.050	1.67	0.64	0.15	7.20
2	30	0.075	1.65	0.80	0.19	5.87
3	30	0.100	1.63	0.92	0.22	5.20
4	30	0.125	1.60	1.02	0.25	4.81
5	30	0.150	1.58	1.12	0.27	4.47

ε_t, c, and k are all values associated with the aimed profile and are not from experimental recordings.

Recorded water surface elevation data at 1.5 m from the initial position of the wave-paddle ($x = 5h$) are presented in Fig. 5.2. Graphs are plotted for the relative water surface elevation, η/a_t, (vertical coordinate axes) versus the dimensionless time, $t\sqrt{g/h}$, (horizontal coordinate axes). In these graphs, thick solid lines represent the recorded waveforms, and thin solid lines represent the aimed profiles of depression solitary waves defined by Eqn. 5.1. As can be seen from this figure, generated depressions are followed by a long, small-amplitude elevation trailing wave. Once a depression forms and starts to detach from the wave paddle, creation of this trailing wave is inevitable due to the deceleration of the wave paddle to a complete stop. This process was visualized by recording a high-speed video for the motion of the wave paddle.

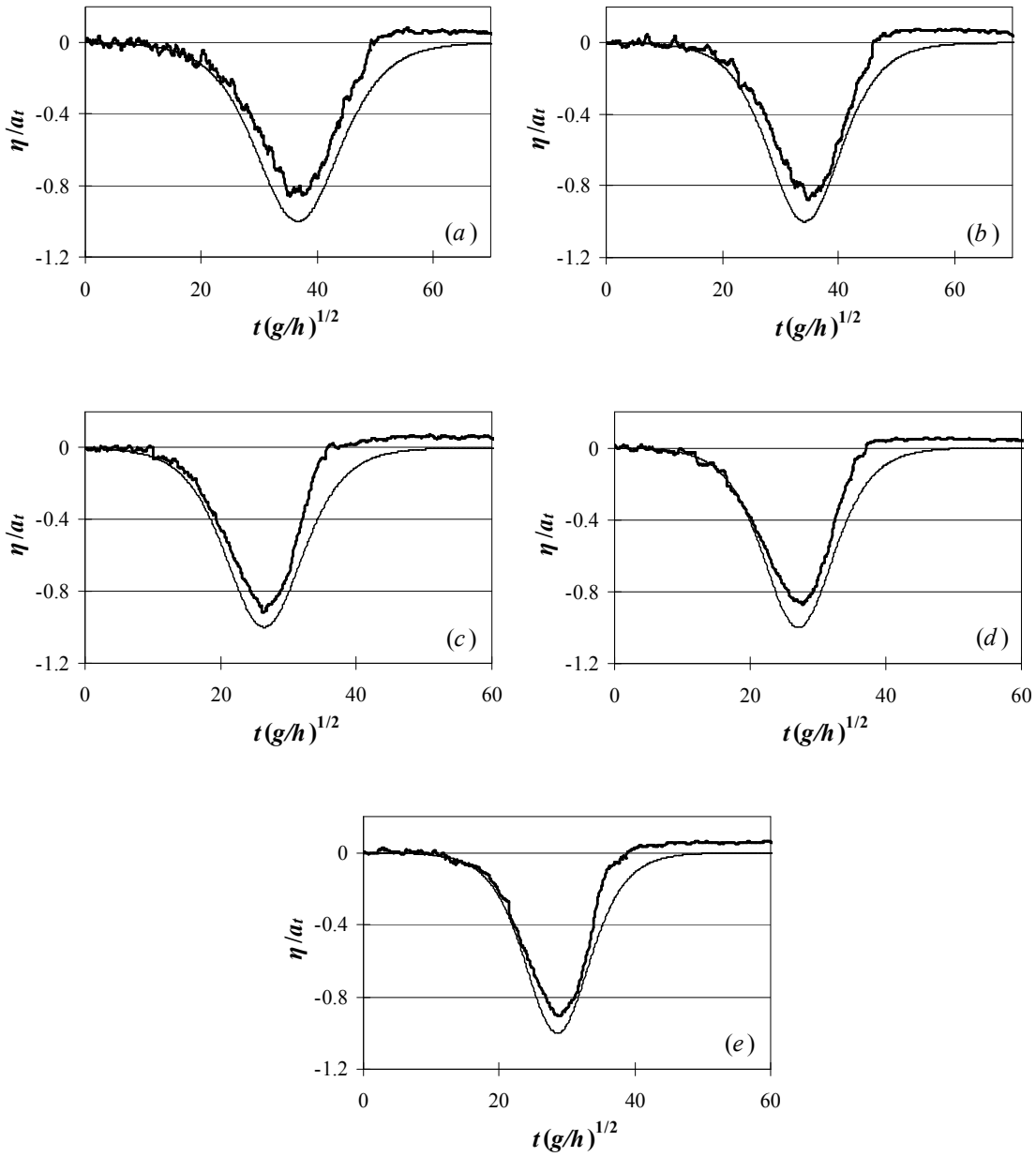

Figure 5.2 Generation of water surface depressions. Wave elevation data recorded at $x = 5h$ (1.5 *m* from the wave paddle) in still water depth of 30 *cm*. (*a*) aimed $\varepsilon_t = a_t/h = 0.05$, (*b*) aimed $\varepsilon_t = 0.075$, (*c*) aimed $\varepsilon_t = 0.1$, (*d*) aimed $\varepsilon_t = 0.125$, (*e*) aimed $\varepsilon_t = 0.15$. Recorded water surface elevation (——); aimed depression solitary wave profile (—).

The amplitude of the trailing wave increases as the waveform propagates until it splits up into a series of oscillatory trailing waves due to the frequency dispersion process which is clearly seen in Figs. 5.3 through 5.5 for the similar experiments conducted in a water depth of 10 *cm*. These trailing waves propagate slower than the main depression. Therefore, the rear edge of the depression adjusts itself to maintain the slower propagation speed of the trailing waves. A similar phenomenon is observed during the generation of elevation solitary waves as described in Chapter 4. However, in the generation of elevation solitary waves, a trailing depression wave follows the main hump and deforms its rear boundary.

5.2 Propagation of Water Surface Depressions

In order to study the propagation characteristics of water surface depressions, a series of experiments were conducted in three different water depths of 6 *cm*, 10 *cm*, and 15 *cm*. Wave elevation data were recorded at different locations along the wave-tank starting from the wave paddle ($x \approx 0$) upto $x=7$ *m*. Water surface level was recorded using capacitance wave gauges (in the case of 10 *cm* water depth) and a digital video camera (in the case of 6 cm and 10 cm water depths). Aiming for a negative solitary wave profiles, water surface depressions with relative trough amplitude values ranging from 0.1 to 0.6 were generated. Details of the experimental conditions are summarized in Table 5.2.

Table 5.2 Experimental conditions for the propagation of water surface depressions

Exp. Run #	h (cm)	$\varepsilon_t = a_t/h$	c (m/s)	k (m^{-1})	S (m)	T (s)	Measurement Method
1	6	0.1	0.73	4.56	0.043	2.34	Video Camera
2	6	0.2	0.69	6.45	0.062	1.80	Video Camera
3	6	0.4	0.59	9.13	0.088	1.56	Video Camera
4	6	0.5	0.54	10.2	0.098	1.56	Video Camera
5	6	0.6	0.49	11.18	0.107	1.61	Video Camera
6	10	0.20	0.89	3.87	0.103	2.32	Wave gauge
7	10	0.25	0.86	4.33	0.115	2.17	Wave gauge
8	10	0.30	0.83	4.74	0.127	2.08	Wave gauge
9	15	0.2	1.08	2.58	0.155	2.87	Video Camera
10	15	0.4	0.94	3.65	0.219	2.45	Video Camera

ε_t, c, and k are all values associated with the aimed profile and are not from experimental recordings.

Figs. 5.3 through 5.5 present the water surface level data recorded by the wave gauges for the experimental runs # 6 through 8 given in Table 5.2. In these figures, graphs are plotted for the dimensionless water surface elevation, η/h, (vertical coordinate axes) versus the dimensionless time, $t\sqrt{g/h}$, (horizontal coordinate axes). Each graph shown in Figs. 5.3 through 5.5 corresponds to a recording of a different wave gauge along the wave-tank. In these figures, graphs a through g are from the wave gauges starting from the closest wave gauge to the wave paddle that is located at $x = 5h$ (50 cm from the wave

paddle, graph *a*) to the farthest wave gauge that is located at $x = 70h$ (7 *m* from the wave paddle, graph *g*). All wave gauges are located in equal intervals of 1 *m* in between, except for the second wave gauge which is located 1.5 *m* from the first one. The evolution of the generated water surface depression in these successive graphs is clear. The initial graph in all figures, corresponding to the recording of the first wave gauge located at 50 *cm* from the wave paddle, consists of a solitary-like negative wave. The higher the amplitude of the aimed depression, the more pronounced were the oscillatory trailing waves recorded at the first gauge indicating more dispersive waveforms. Water surface level graphs for the experimental runs 1-5, 9, and 10 are presented in the Appendix. For those experiments water surface levels were recorded using a digital video camera and the data were extracted using the procedure outlined in Chapter 3.

Experimental Results

In all the experimental runs, the initial solitary-like depression wave deformed into a triangular-shape depression wave followed by a series of oscillatory trailing waves. As the initial solitary-like depression propagates, the leading half of the depression wave flattens and elongates in the direction of propagation whereas the rear half of the depression becomes steeper. Therefore, the lowest point of the depression gets closer to the rear end of the depression as the depression propagates which makes the depression look more like a triangle.

The experimental celerity of a generated depression wave was estimated by the time elapsed for the depression wave to pass successive wave gauges that are separated with a known distance. Then, c_{exp} was estimated by averaging all the experimental celerities

calculated for each pair of wave gauges. In Fig. 5.6 the dimensionless theoretical celerity, $c_{theo}/\sqrt{gh}$, is plotted against the dimensionless experimental celerity, $c_{\exp}/\sqrt{gh}$. Theoretical celerities were calculated using the equation derived by Korteweg de-Vries (1895) as $c=\sqrt{gh}\left(1-a_t/2h\right)$. Since the amplitude of the depression is decreasing during the propagation, the theoretical celerity, c_{theo}, is estimated by averaging the theoretical celerities at the location of each recording station. In Fig. 5.6, the corresponding experiment numbers (see Table 5.2) are marked adjacent to the symbols. In this figure, the thin dashed line represents the case of a perfect match between the experimental and theoretical celerities. As can be seen from this figure, the celerity of depressions are very close to, yet less than, the celerity of long waves as previously also observed by Hammack and Segur (1978). The theory always underestimates the measured celerity of the generated depression; the greater the relative amplitude of the depression, the greater the error in the theoretical estimation. The celerity of a propagating depression is not constant during the propagation and it slightly increases with distance as the amplitude of the depression decreases. This agrees well with the theoretical trend of the celerity predicted by $c=\sqrt{gh}\left(1-a_t/2h\right)$.

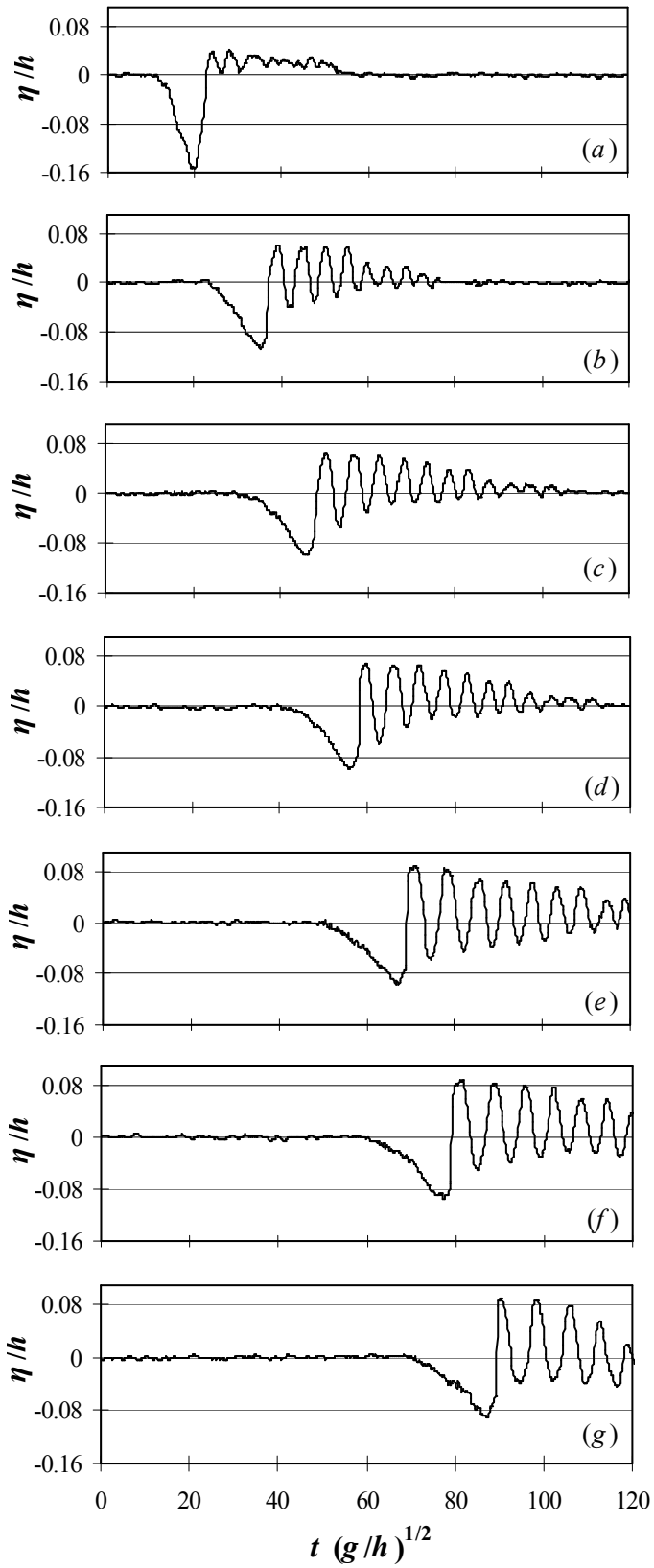

Figure 5.3 Recorded water surface elevation along the wave-tank, $\varepsilon_t = 0.2$, $h = 10$ *cm* (*a*) $x/h = 5$, (*b*) $x/h = 20$, (*c*) $x/h = 30$, (*d*) $x/h = 40$, (*e*) $x/h = 50$, (*f*) $x/h = 60$, (*g*) $x/h = 70$

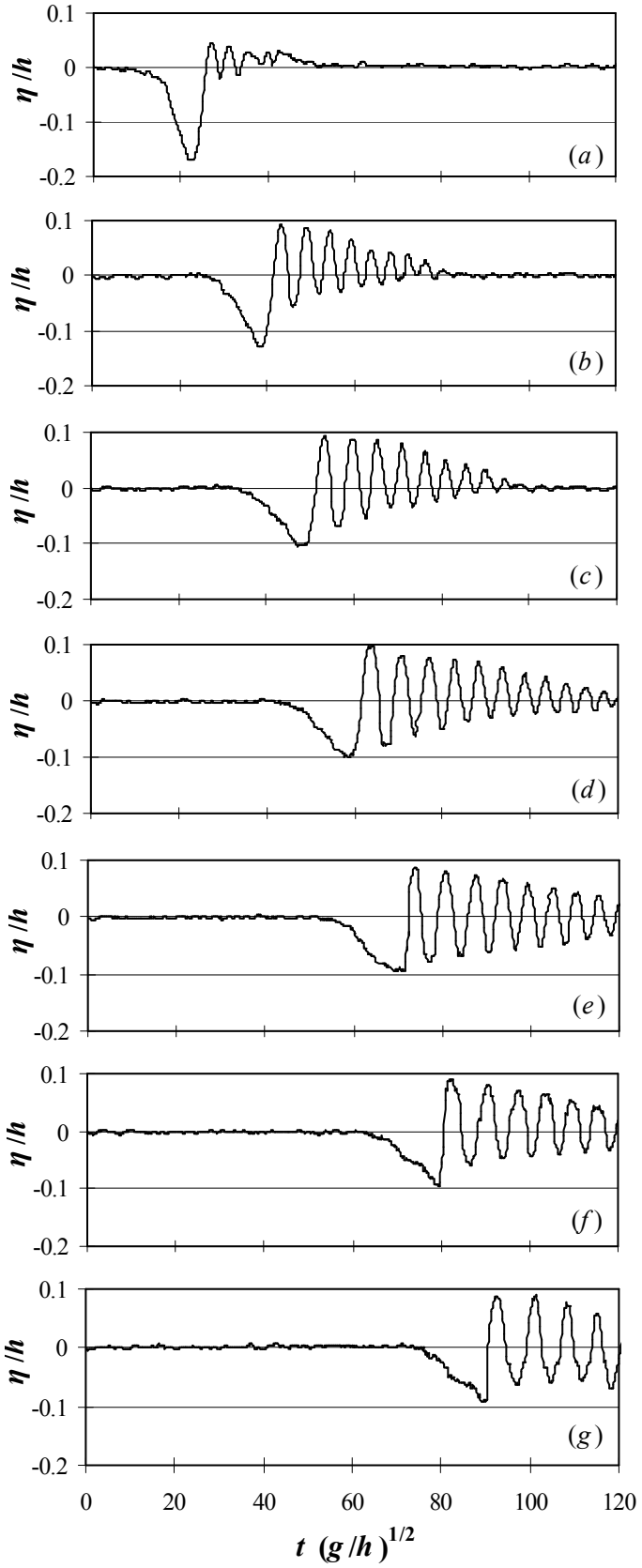

Figure 5.4 Recorded water surface elevation along the wave-tank, $\varepsilon_t = 0.25$, $h = 10$ *cm* (*a*) $x/h = 5$, (*b*) $x/h = 20$, (*c*) $x/h = 30$, (*d*) $x/h = 40$, (*e*) $x/h = 50$, (*f*) $x/h = 60$, (*g*) $x/h = 70$

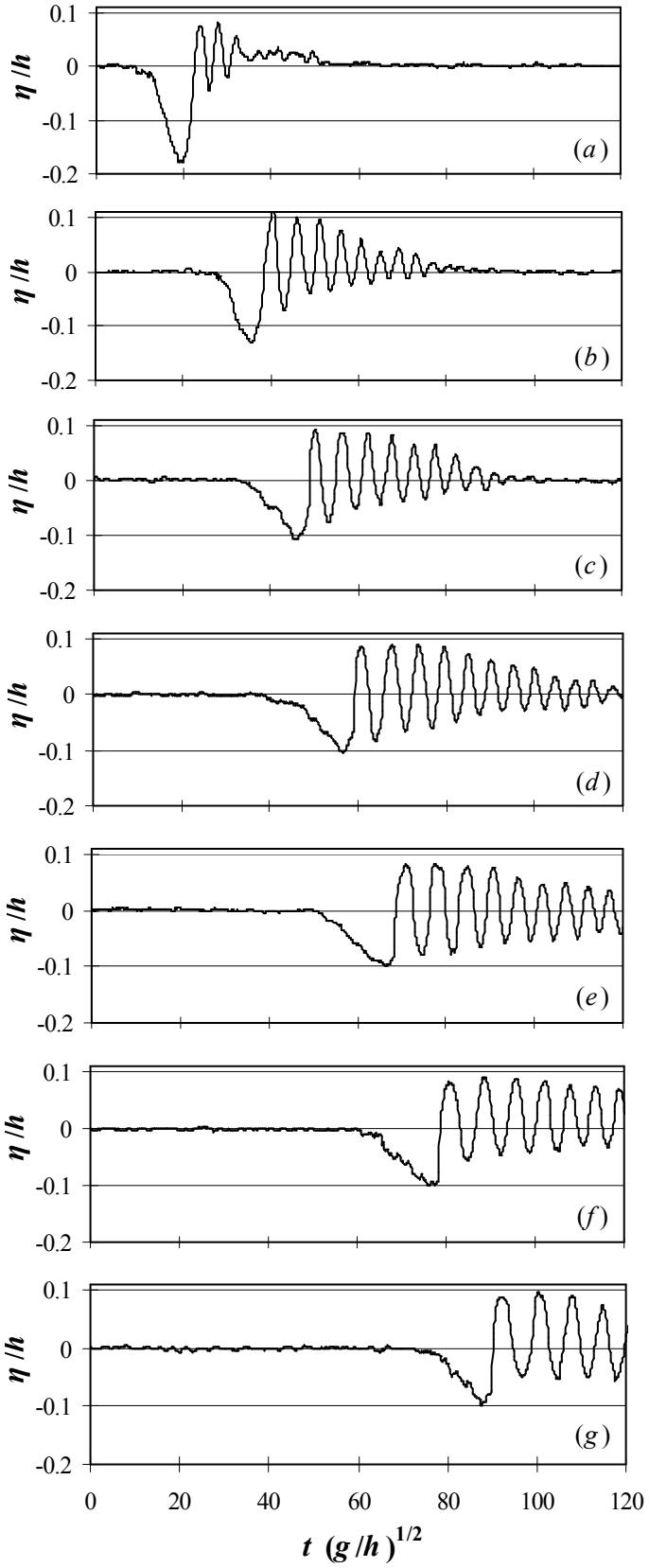

Figure 5.5 Recorded water surface elevation along the wave-tank, $\varepsilon_t = 0.3$, $h = 10$ *cm* (*a*) $x/h = 5$, (*b*) $x/h = 20$, (*c*) $x/h = 30$, (*d*) $x/h = 40$, (*e*) $x/h = 50$, (*f*) $x/h = 60$, (*g*) $x/h = 70$

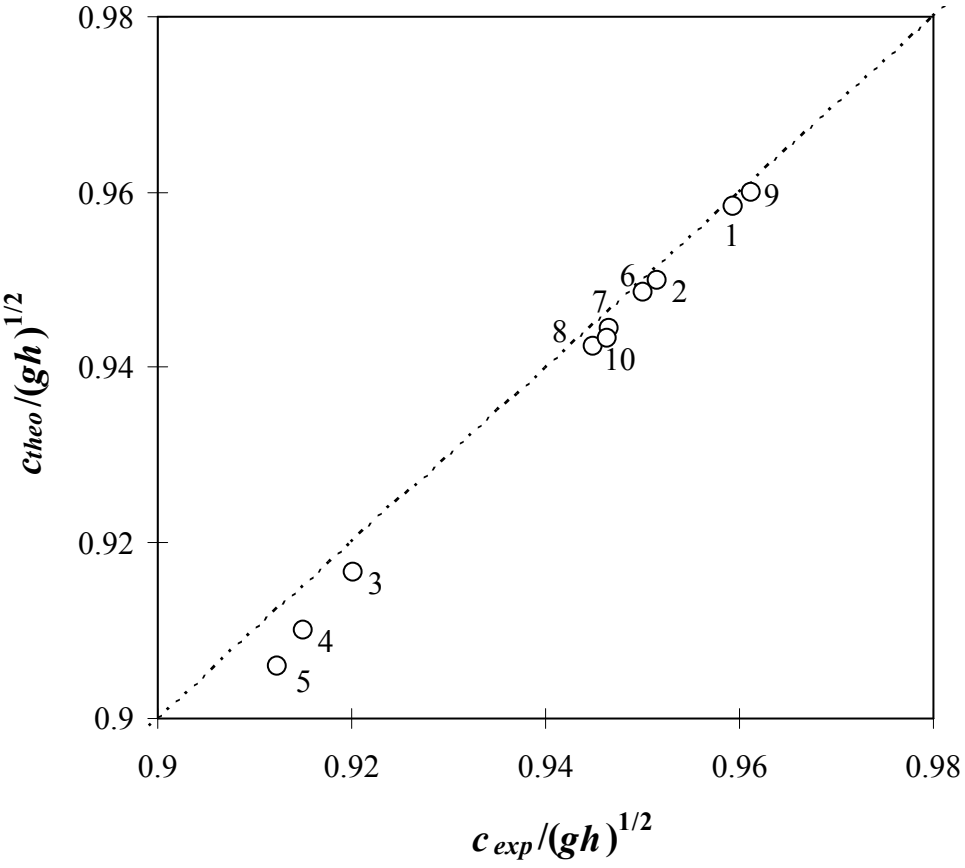

Figure 5.6 Comparison of averaged experimental and theoretical celerities of the generated water surface depressions. Numbers adjacent to the symbols indicate the number of experiment as given in Table 5.2. Thin dashed line represents the line of equal experimental and theoretical celerity values.

As stated earlier, the profile of a propagating depression includes three main parts: a leading limb, a rear limb, and a series of oscillatory trailing waves. The leading half can be approximated by half of a negative solitary wave profile. In order to estimate the boundary decay coefficient of the leading edge, half of a negative solitary wave profile with a general function of Eqn. 5.5 has been fitted to the leading half of the recorded waveform.

$$\eta = - a_{t\text{-}reg}\, sech^2\, [k_{exp}\, c_{exp}(t\text{-}t_0)] \qquad (5.5)$$

By performing a curve fitting analysis and using the least squares method, the three unknowns of the wave profile given by Eqn. 5.5 [i.e., the leading boundary decay coefficient, k_{exp}, the amplitude of depression, $a_{t\text{-}reg}$, and the time constant, t_0] are determined for each experimental run and at all individual recording stations. Eqn. 5.5 is fitted to the bottom 95% (i.e., depression elevation values larger than 5% of the trough height) of the recorded wave elevation data. The main reason for choosing the bottom 95% of the wave elevation data is the problem of contamination of the top 5% of the recorded waveforms by the noise signals, especially in the case of low amplitude troughs. Result of a typical fitting analysis is presented in Fig. 5.7. Values of k_{exp} for the leading half of the generated depressions observed at different locations along the wave-tank are presented in Fig. 5.8*a*. In this figure, the dimensionless boundary decay coefficient, kh, is graphed against the dimensionless distance from the wave paddle, x/h for all experimental runs. As can be seen in this figure, the larger the trough amplitude, the faster the change in the leading half toward a flatter profile. After an initial rapid change in the profile shape (until approximately $x = 30h$), the rate of change decreases considerably in all cases. However, there is always a tendency toward elongation and a smoother profile in the leading half of the waveform due to nonlinear dispersion processes.

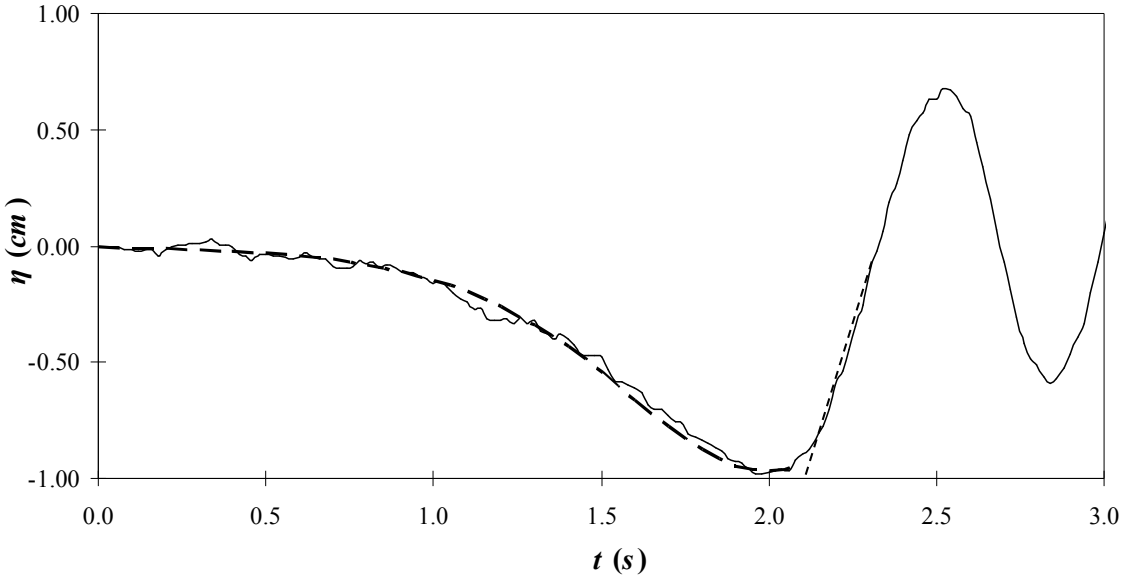

Figure 5.7 A typical curve fitting analysis to determine the length characteristics in the leading and rear halves of generated depression. The waveform is from Exp. #9 and recorded by the fourth wave gauge at x = 4 m. (——) - recorded wave elevation data, (— — —) - best fitted curve to the leading half of the recorded profile, (– – –) - best fitted line to the rear half of the recorded profile.

Ursell number, *Ur*, governs the relative importance of linear effects of frequency dispersion versus nonlinear effects of amplitude dispersion in the propagation of waveforms. For Ursell numbers that are much larger than unity, $Ur >> 1$, nonlinear effects govern the wave propagation whereas for Ursell numbers that are much smaller than unity, $Ur << 1$, linear effects govern the wave propagation. For values of *Ur* close to unity, both linear and nonlinear factors contribute to the wave propagation to some extent and therefore, both effects should be taken into account. For the leading half of the propagating depression, *Ur* number can be defined as:

$$Ur = \frac{a_t / h}{(h/L)^2} = \frac{a_t l^2}{h^3} \tag{5.6}$$

where l is the length characteristic of the leading half of the waveform in the direction of propagation. The length of a solitary wave of elevation or depression is theoretically infinite. However, for practical purposes, since the water surface elevation becomes zero reasonably fast with x (see Eqn. 5.5), an effective length, L, (for a similar definition of effective length of a solitary wave see Grimshaw, 1971) can be defined as:

$$L = \frac{2\cosh^{-1}(10)}{k} \tag{5.7}$$

In Eqn. 5.7, L has been determined such that at $x = L$, $\eta/h = 0.01$. The length characteristic of the leading half of a solitary wave, l, is half of L determined using Eqn. 5.7.

Elongation of the depression from its frontal edge manifests the increase of nonlinear effects in the leading half of the propagating waveform. To further investigate the rate of change in the Ursell number and consequently the rate of change in the importance of nonlinear effects on the wave propagation, Ursell numbers for the leading halves of the propagating depressions at different locations along the tank are estimated for all experimental runs. In Fig. 5.8*b*, Ur is sketched versus dimensionless distance, x/h, for all runs.

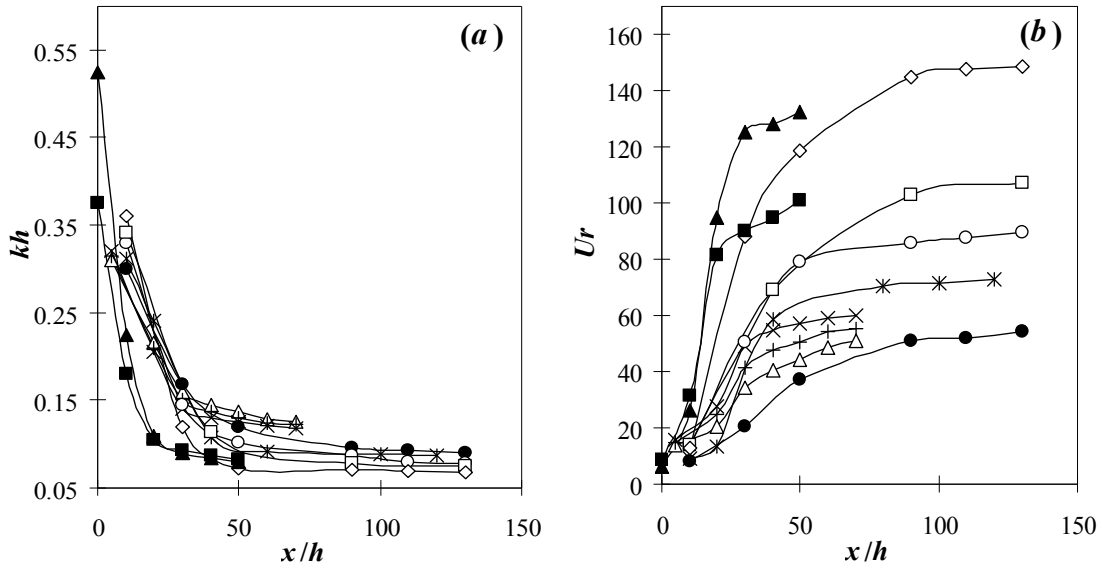

Figure 5.8 (*a*) Experimental outskirt boundary decay coefficient of the leading edge, k_{exp}, (*b*) Ursell number of the leading half. (—●—) Exp. #1, ε_t = 0.1, h = 6 *cm*, (—*—) Exp. #2, ε_t = 0.2, h = 6 *cm*, (—○—) Exp. #3, ε_t = 0.4, h = 6 *cm*, (—□—) Exp. #4, ε_t = 0.5, h = 6 *cm*, (—◊—) Exp. #5, ε_t = 0.6, h = 6 *cm*, (—Δ—) Exp. #6, ε_t = 0.3, h = 10 *cm*, (—+—) Exp. No. 7, ε_t = 0.25, h = 10 *cm*, (—×—) Exp. No. 8, ε_t = 0.3, h = 10 *cm*, (—■—) Exp. No. 9, ε_t = 0.3, h = 15 *cm*, (—▲—) Exp. No. 10, ε_t = 0.3, h = 15 *cm*.

By the reduction in the boundary decay coefficient (thus, elongation) of the leading half of the propagating depression, the effects of nonlinearity in the propagation of the leading half are enhanced. While *Ur* always increases as the wave propagates, the rate of increase in *Ur*, (thus, the rate of increase in nonlinear effects) slows down with distance. For very large values of *Ur*, linear effects of frequency dispersion can be neglected in the propagation of the leading half of a depression.

In order to estimate the Ursell number for the rear half of the propagating depression, l is assumed to be the distance from the lowest elevation point of the trough to the point

where the profile intersects with the still water level. The change in l and Ur with distance for the rear halves of the generated depressions are plotted in Figs. (5.9*a*) and (5.9*b*), respectively.

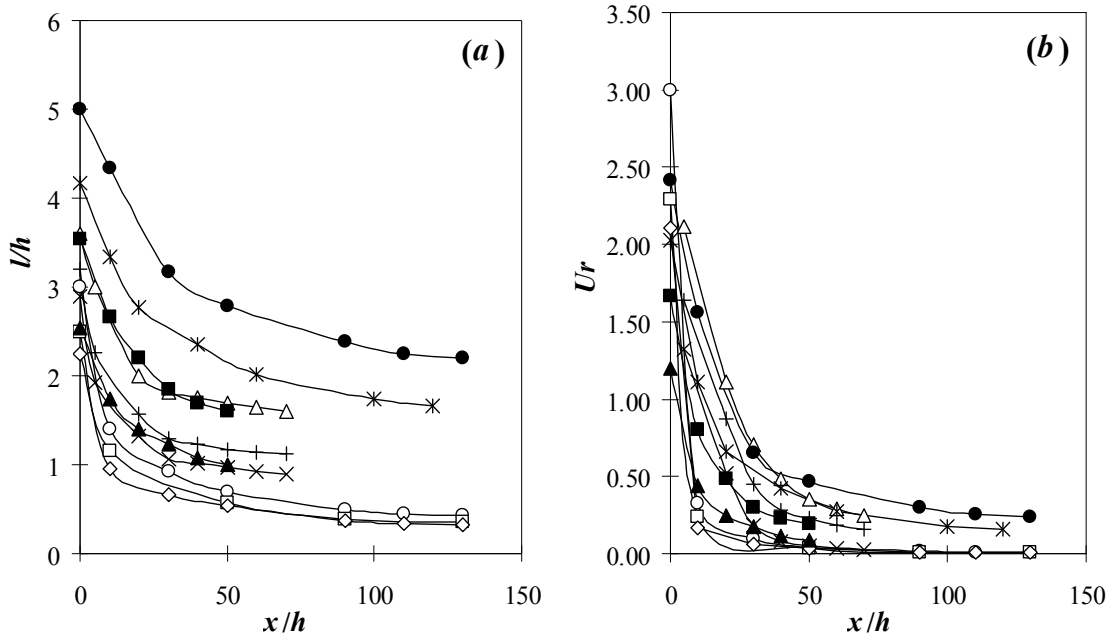

Figure 5.9 (*a*) Experimental length characteristic of the rear half, *l*. (*b*) Ursell number of the rear edge. (—●—) Exp. #1, $\varepsilon_t = 0.1$, $h = 6$ *cm*, (—*—) Exp. #2, $\varepsilon_t = 0.2$, $h = 6$ *cm*, (—○—) Exp. #3, $\varepsilon_t = 0.4$, $h = 6$ *cm*, (—□—) Exp. #4, $\varepsilon_t = 0.5$, $h = 6$ *cm*, (—◊—) Exp. #5, $\varepsilon_t = 0.6$, $h = 6$ *cm*, (—Δ—) Exp. #6, $\varepsilon_t = 0.3$, $h = 10$ *cm*, (—+—) Exp. # 7, $\varepsilon_t = 0.25$, $h = 10$ *cm*, (—×—) Exp. # 8, $\varepsilon_t = 0.3$, $h = 10$ *cm*, (—■—) Exp. # 9, $\varepsilon_t = 0.3$, $h = 15$ *cm*, (—▲—) Exp. # 10, $\varepsilon_t = 0.3$, $h = 15$ *cm*.

As can be seen from Fig. 5.9a, the characteristic length of the rear half in a generated depression decreases as it propagates. The reduction rate is faster initially and slows down gradually with distance. The Ursell number in the rear half also decreases as the depression propagates along the wave-tank as shown in Fig. 5.9*b*. Similarly, the reduction rate is higher at the outset and diminishes with distance.

Significant amplitude attenuation of the generated depression waves is observed. This attenuation is due to viscous and dispersive effects. As discussed in Chapter 4, Keulegan (1948) proposed the following analytical parameterization to predict the attenuation of solitary wave's amplitude in channels due to bottom and sidewall frictional effects:

$$\left(\frac{H_2}{h}\right)^{-1/4} = \left(\frac{H_1}{h}\right)^{-1/4} + \frac{1}{12}\left(1+\frac{2h}{b}\right)\frac{x}{h}\sqrt{\frac{\upsilon}{g^{1/2}h^{3/2}}} \tag{4-15}$$

Elevation solitary waves are in weakly nonlinear and weakly dispersive regimes; therefore, damping of the amplitude is mainly governed by viscous frictional effects rather than dispersive effects. However, water surface depressions are fully nonlinear and fully dispersive waveforms, and dispersive effects are of primary importance for amplitude attenuation. During the propagation of a depression wave both linear dispersive effects (known as frequency dispersion) and nonlinear effects (known as amplitude dispersion) contribute to the reduction of the wave amplitude. Fig. 5.10 illustrates the attenuation of depressions' amplitude with distance for the experimental runs # 6 - 8 (see Table 5.2). In this figure, solid lines with symbols represent the attenuation curves extracted from the recorded wave elevation data at different stations along the wave-tank. Graphs are plotted for the dimensionless depression amplitude a_t/a_{t0} (vertical coordinate axes, a_t is the measured depression amplitude along the wave-tank, and a_{t0} is the measured depression amplitude at the wave-paddle) versus dimensionless distance along the wave-tank, x/h (horizontal coordinate axes). Initially, generated waves are highly dispersive, leading to a rapid attenuation of amplitudes with distance as shown in Fig. 5.10. However, it can be seen that the dispersive effects diminish as the waves propagate further along the tank (approximately a distance of 30h - 40h from the wave paddle) as indicated by the decrease in the damping rate of the

amplitudes. Once the depressions propagate through this initial region, the rate of attenuation slows down; however, it is still larger than Keulegan's predictions. This indicates the ongoing contribution of the dispersive effects during the rest of the wave propagation.

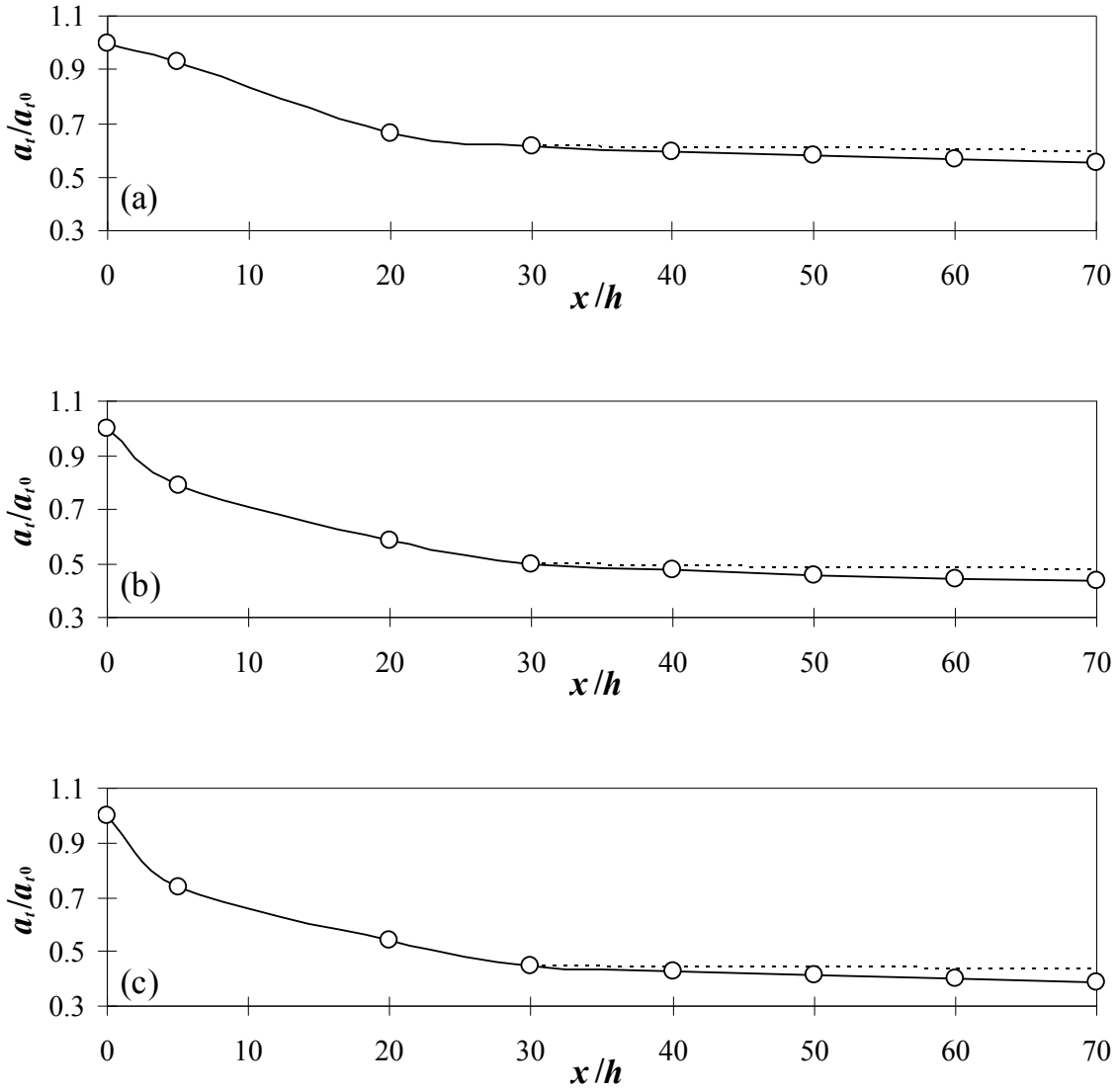

Figure 5.10 Amplitude attenuation of the water surface depressions along the wave-tank. (*a*) Exp. #6, $\varepsilon_t = 0.2$, $h = 10$ *cm*, (*b*) Exp. #7, $\varepsilon_t = 0.25$, $h = 10$ *cm*, (*c*) Exp. #8, $\varepsilon_t = 0.3$, $h = 10$ *cm*. (–○–) Attenuation curve; (- - -) Keulegan's prediction.

Parameterization

In this section the efforts to parameterize the shape of the depression wave profile are presented. The depression waves are treated of being composed of two parts: leading and rear halves as discussed before. The leading half is considered to be a negative solitary-like wave and the rear half is considered to be a straight line. Therefore, parameterization for the depression amplitude, frequency (hence, boundary decay coefficient), and rear half slope is needed for a propagating depression wave.

The primary parameters of interest for the propagation of water surface depressions are: the initial amplitude of the depression at x=0, a_{t0}; the stationary water depth, h; the gravitational acceleration, g; the propagation distance of the generated wave, x; the dynamic viscosity of the water, υ; and the amplitude of the depression at the distance x from the wave paddle a_t. By performing a dimensional analysis (for details of the dimensional analysis see Malek-Mohammadi and Testik (2009*b*)), four important dimensionless parameters are identified as: (i) the relative amplitude of the depression, a_t/a_{t0}; (ii) the dimensionless distance traveled by the depression, x/h; (iii) the initial dimensionless wave amplitude, $\varepsilon_{t0} = a_{t0}/h$; and (iv) the dimensionless viscous diffusion velocity, $\upsilon/(g^{1/2} h^{3/2})$.

Experimental data collected in the present study together with the experimental data reported by Hammack and Segur (1978) are used to perform a fitting analysis as shown in Fig. 5.7 to determine the depression amplitudes, boundary decay coefficients for the leading halves, and the slopes of the rear halves of the depression waves at different

locations along their propagation path. Consequently, the following empirical equation for the attenuation of water surface depressions is proposed:

$$\left(\frac{a_t}{a_{t0}}\right)^{-1/4} = 1 + 26.6\left(\frac{x}{h}\right)^{1/3}\left(\frac{a_{t0}}{h}\right)^{2/3}\left(\frac{\upsilon}{g^{1/2}h^{3/2}}\right)^{2/3} \tag{5.8}$$

Experimental data and the predictions of Eqn. 5.8 are presented in Fig. 5.11. As can be seen from this figure, estimations using the proposed parameterization are in good agreement with the experimental data collected in this study and the study by Hammack and Segur (1978) with the R^2 value of 0.96.

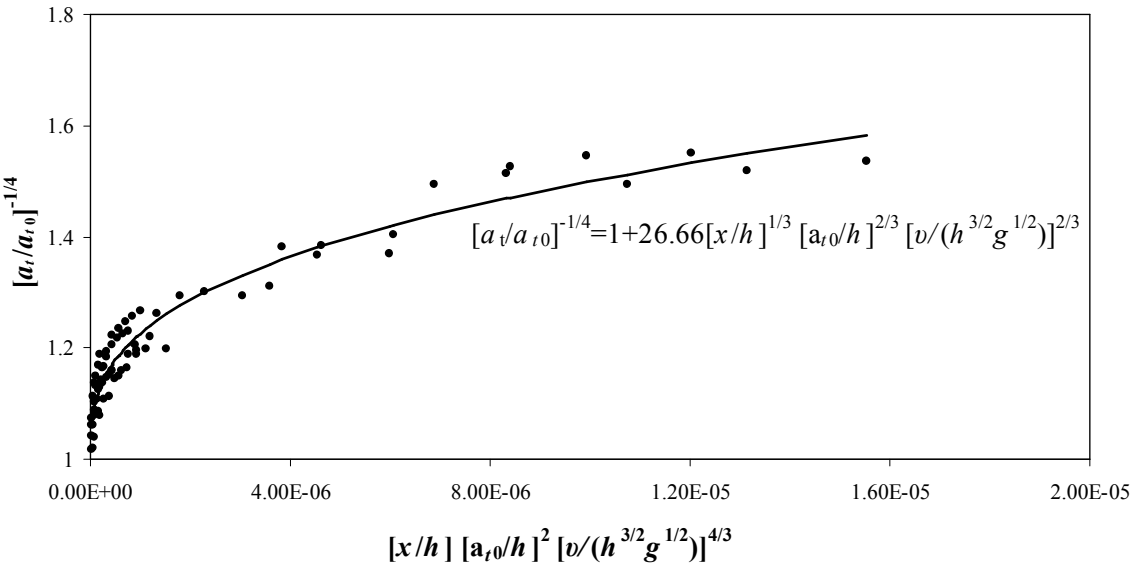

Figure 5.11 Comparison of the experimental data and the estimations by Eqn. 5.8 for the attenuation of a water surface depression. (●) experimental data, (——) estimations.

By performing a similar analysis (for details see Malek-Mohammadi and Testik (2009*b*)), the important dimensionless governing the depression wave profile shape are identified as the dimensionless frequency of the leading half, $\Omega a_t/(gh)^{1/2}$, the dimensionless distance traveled by the depression, x/h, the dimensionless viscous diffusion velocity, $\upsilon/(g^{1/2}\, h^{3/2})$, and the Froude number $c/(gh)^{1/2}$. Experimental data reported in the present study together with the experimental data presented by Hammack and Segur (1978) are plotted in Fig. 5.12. The following empirical equation for the frequency of the leading edge of the propagating water surface depression is proposed:

$$\frac{\Omega a_t}{\sqrt{gh}} = 2.1\left(\frac{x}{h}\right)^{-2/3}\left(\frac{\upsilon}{h^{3/2}g^{1/2}}\right)^{1/4} \tag{5.9}$$

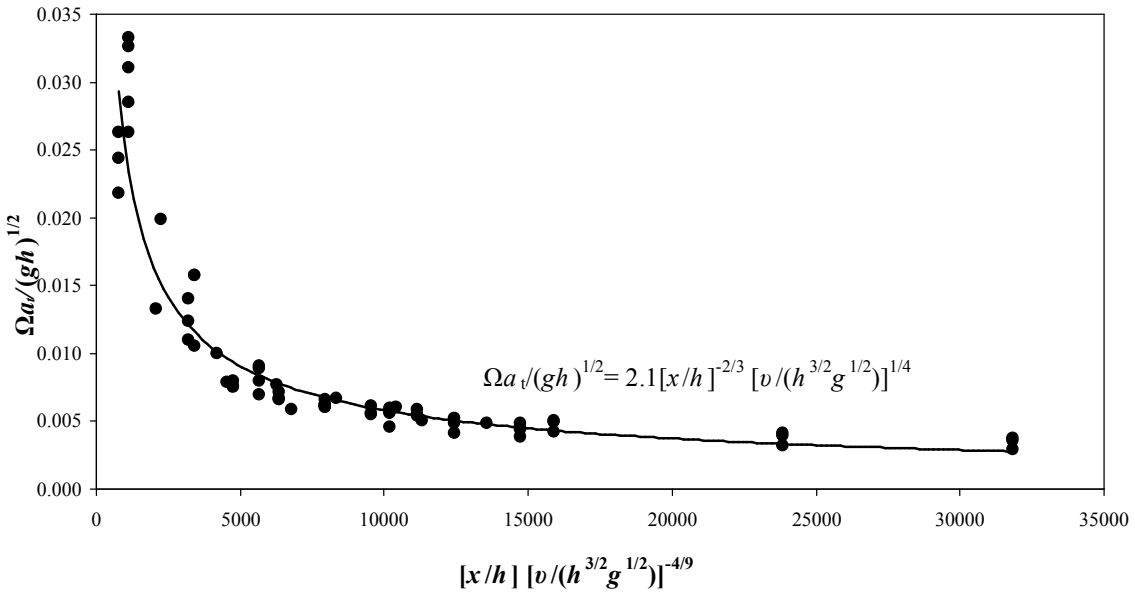

Figure 5.12 Comparison of the experimental data and the estimations of Eqn. 5.9 for the boundary shape of the leading half of propagating water surface depressions. (●) experimental data, (——) estimations.

As can be seen from this figure, estimations using the proposed parameterization are in good agreement with the experimental data collected in this study and the study by Hammack and Segur (1978) with the R^2 value of 0.94.

Finally, a similar analysis is performed to identify the following important dimensionless parameters for the slope of the rear half of a propagating depression: the relative slope of the rear boundary, S/S_0, (S – slope after a particular propagation distance, S_0 – initial slope at the wave paddle); the dimensionless viscous diffusion velocity, $\upsilon/(g^{1/2} h^{3/2})$; the dimensionless amplitude of the depression at a distance x from the wave paddle, a_t/h; and the dimensionless distance traveled by the depression, x/h. Experimental data collected in the present study together with the experimental data presented by Hammack and Segur (1978) are shown in Fig. 5.13. The following empirical parameterization for the slope of the rear edge of the propagating water surface depression is proposed:

$$\frac{S}{S_0} = 0.015\left(\frac{x}{h}\right)^{1/3}\left(\frac{a_t}{h}\right)^{1/6}\left(\frac{\upsilon}{h^{3/2}g^{1/2}}\right)^{-1/6} \tag{5.10}$$

As can be seen from this figure, estimations using the proposed parameterization are in good agreement with the experimental data collected in this study and the study by Hammack and Segur (1978) with the R^2 value of 0.93.

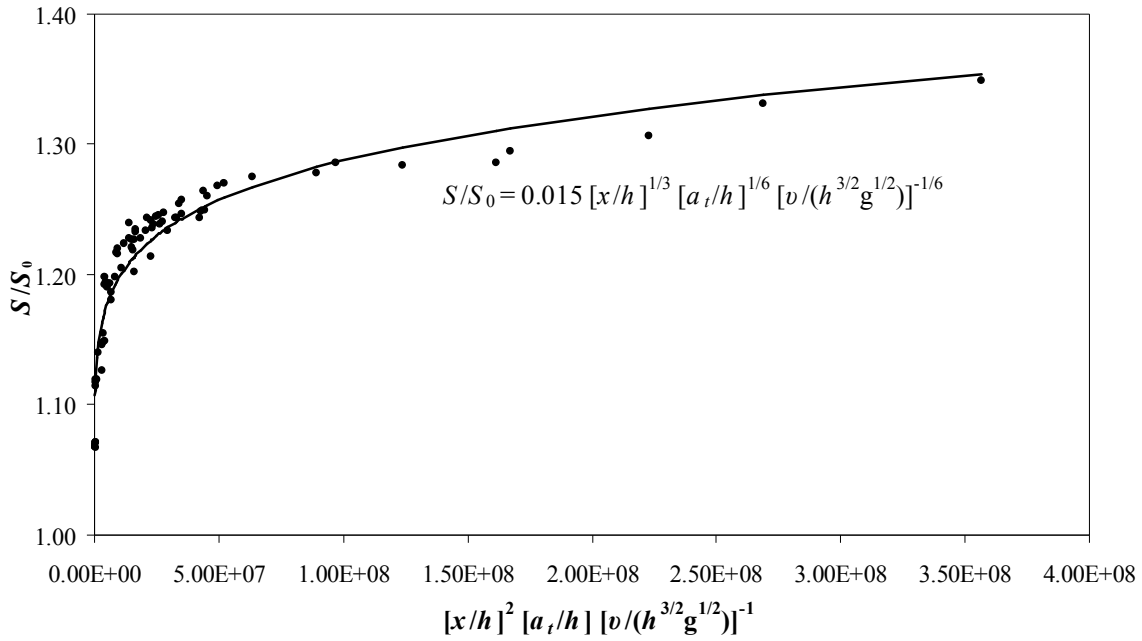

Figure 5.13 Comparison of the experimental data and the estimations by Eqn. 5.10 for the slope of the rear half of a propagating water surface depression. (●) experimental data, (——) fitted curve.

CHAPTER SIX

CONCLUSIONS

In the present study, solitary waves and water surface depressions representing two common components of a typical tsunami profile were generated in a laboratory wave-tank. Furthermore, physics of propagation of these two waveforms (i.e. profile shape evolutions, amplitude attenuation, and propagation celerity) were studied in detail. In this Chapter, major conclusions drawn from the present study that are discussed in Chapters 4 and 5 are summarized and possible future research directions are briefly discussed.

Solitary waves

As previously argued by Synolakis (1990), the traditional methodology proposed by Goring (1979) does not take into account the evolving nature of the wave during the formation. In other words, it considers an established profile of a solitary wave and its characteristics, such as celerity, even during the generation process. Motivated by this discrepancy, a New methodology for laboratory generation of solitary waves using piston-type wavemakers is proposed. The most important difference between the proposed New methodology and the traditional methodology by Goring (1979) is the consideration of the evolving nature of the wave during the generation process. In this New methodology, the celerity of the wave during the formation process is not assumed to match the celerity of an established solitary wave; rather it is assumed that the celerity depends on the amplitude of an unsteady water surface elevation component that accumulates in front of the wave paddle at each time step. The celerity of the elevation

component and the velocity of the wave paddle at each time step are determined by mass and momentum conservation considerations. Through a series of experiments, it was demonstrated that the New methodology is capable of generating more accurate waves in terms of wave height and profile shape compared to the Goring methodology. It even produces highly accurate waves closer to the wave paddle. Smaller trailing waves are observed in the generated waveforms compared to those generated by the Goring methodology.

Solitary waves generated by the New methodology are established in a distance of approximately 10*h* and 20*h* from the wave paddle for Rayleigh-type and Boussinesq-type profiles, respectively. The establishment of Rayleigh-type solitary waves generated by the Goring methodology occurs after a distance of 30*h* from the wave paddle. The complete establishment of Boussinesq-type solitary waves generated by the Goring methodology occurs at a distance larger than 70*h* from the wave paddle. However, due to the limitations associated with the size of the wave-tank, completely established Boussinesq-type waves were not observed in the present study. The establishment rate of solitary waves is especially important in tsunami research because faster establishment rates make it possible to study tsunamis in shorter and smaller wave-tanks, whereas ordinarily tens of meters of length is required.

Amplitude attenuation of solitary waves generated by the New methodology can be better explained by the viscous frictional damping formulas proposed by Keulegan (1948) compared to the waves generated by the Goring methodology. Theoretical solitary waves

are in weakly nonlinear weakly dispersive regime; therefore, their profile shape does not change with propagation distance. Solitary waves generated by the Goring methodology attenuate faster with distance than the Keulegan's prediction indicating the pronounced dispersive nature of the generated waves. This condition is more pronounced in the case of Boussinesq-type waves.

Boussinesq-type waves are followed by larger trailing waves compared to Rayleigh-type waves. Moreover, trailing waves are attached to the main hump for a longer distance in the case of Boussinesq-type waves. These and the alternative definition of the outskirt decay coefficient in Boussinesq solution make Boussinesq-type waves more nonlinear and more dispersive compared to Rayleigh-type waves. This is believed to be responsible for the severe attenuation of Boussinesq-type generated waves.

The generated solitary wave profile is always followed by a very long and small-amplitude water surface depression which consists of a series of oscillatory trailing waves. The propagation speed of the trailing depression is lower than the celerity of the main hump slowing down the movement of the main hump and deforming its rear boundary. With the New methodology, trailing waves detach faster from the rear boundary of the main hump. Faster detachment of the trailing waves reduces the nonlinearity of the waveform, diminishes large dispersive effects, and consequently reduces wave transformations during propagation.

Waves generated by the New methodology propagate with celerity values closer to the theoretical values than the waves generated by the Goring methodology for the full range of relative amplitudes studied.

Depression waves

Negative solitary-like depression waves are generated in the wave-tank using the Goring methodology. Once the depression waves are generated, they immediately start deforming both in terms of amplitude and profile shape. As the depression wave propagates, its amplitude attenuates due to nonlinear and dispersive effects as well as due to frictional damping. The frontal edge of the depression elongates while its rear boundary steepens with distance. Because of linear dispersion effects, oscillatory trailing waves emerge from the tail of the depression wave. Oscillatory trailing waves consist of both negative (below stationary water level) and positive (above stationary water level) components. Negative and positive components are not completely symmetrical about the stationary water level as the amplitudes of the positive components are generally larger than the amplitudes of the negative components. The length of oscillatory trailing waves increases with distance. The greater the distance propagated by the depression, the greater the number of positive and negative components in the oscillatory wave train. The closest components to the depression in the oscillatory wave train have the largest positive and negative amplitudes, and the amplitudes of other components decrease almost linearly as their distance to the main depression increase. The amplitudes of the oscillatory trailing waves increase with the distance propagated by the main depression initially, and then start decreasing due to viscous and dispersive effects. After some

propagation distance, the initial oscillatory trailing wave group splits up into two oscillatory trailing wave groups. Given the size limitations of the wave-tank used in this study, this phenomenon was only observed in the case of steep water surface depressions. For the small-amplitude depressions, this process was not observed during the experiments within the length of the set-up. The formation of oscillatory trailing waves is hastened in the case of steep water surface depressions. The profile of individual positive and negative components in the oscillatory wave train is steeper in the case of steep water surface depressions. As the waveform propagates, the profile of individual components in the oscillatory wave train elongates, and therefore the profiles of the individual components become flatter.

The celerity of a depression wave increases gradually with distance; however, it is always lower than the celerity of long waves in deep water. This increase in the celerity with distance may partially be attributed to the decrease in the trough amplitude. In our analysis, the depression waves are treated of being composed of two parts: leading and rear halves. The leading half is considered to be a negative solitary-like wave and the rear half is considered to be a water surface that can be simply modeled by a straight line. Therefore, using the experimental data of the present study and those reported by Hammack and Segur (1978), three empirical parameterizations are proposed for the prediction of depression amplitude, a_t, frequency (hence, boundary decay coefficient) of the leading half, Ω, and slope of the rear half, S, as the waveform propagates. These parameterizations are as follows:

$$\left(\frac{a_t}{a_{t0}}\right)^{-1/4} = 1 + 26.6\left(\frac{x}{h}\right)^{1/3}\left(\frac{a_{t0}}{h}\right)^{2/3}\left(\frac{\upsilon}{g^{1/2}h^{3/2}}\right)^{2/3} \tag{5.8}$$

$$\frac{\Omega a_t}{\sqrt{gh}} = 2.1\left(\frac{x}{h}\right)^{-2/3}\left(\frac{\upsilon}{h^{3/2}g^{1/2}}\right)^{1/4} \tag{5.9}$$

$$\frac{S}{S_0} = 0.015\left(\frac{x}{h}\right)^{1/3}\left(\frac{a_t}{h}\right)^{1/6}\left(\frac{\upsilon}{h^{3/2}g^{1/2}}\right)^{-1/6} \tag{5.10}$$

Future Research Direction

Eyewitness reports of recent tsunami events indicate that typical nearshore profile of a tsunami consist of both elevation and depression components. Based on these field observations and numerical simulations, two main configurations for the nearshore profile of a tsunami are considered as Leading Depression N-wave (LDN) and Leading Elevation N-wave (LEN). Future research needs to be focused on the laboratory investigation of these waveforms composed of combined elevation and depression components. This present study on the propagation of individual elevation and depression components representing the two parts of a tsunami waveform should be extended to include the interaction between the elevation and depression components of the wave during the propagation.

Tsunamis are not always propagating over horizontal bottoms as in deep oceans; but they also propagate over the continental slope and more specifically they climb up the beach slope. While the propagation of solitary waves over sloping bottoms have long been studied experimentally (Madsen and Mei, 1969; Camfield and Street, 1969; Skjelbreia,

1987; Synolakis, 1987; Zelt, 1991; Grilli et al., 1994; Grilli et al., 2004 and many others), no experimental studies have been reported on the propagation of water surface depressions or combined profiles of depression and elevation components such as N-waves over sloping bottoms. Future research needs to consider the effect of sloping bottom on the propagation of water surface depressions and combined profiles of depression and elevation components.

REFERENCES

Berkman, S. C., Symons, J. M., (1960). "The tsunami of May 22, 1960 as recorded at tide stations," U.S. Department of Commerce, Coast and Geodetic Survey, Washington, DC, 76 pp

Borrero, J., M. Ortiz, V. Titov, and C.E. Synolakis (1997): Field survey of Mexican tsunami produces new data, unusual photos. *Eos Trans. AGU, 78*(8), 85, 87–88.

Boussinesq M.J., (1871). "Théorie de l'intumescence liquide, appelée onde solitaire ou de translation, se propageant dans un canal rectangulaire," C.-R. Acad. Sci. Paris, 72p.

Byatt-Smith J.G.B., (1970). "An exact integral equation for steady surface waves," *Proc. Roy. Soc. London, A.* 315, p 405-418.

Byatt-Smith, J. G., (1971). "An integral equation for unsteady surface waves and a comment on the Boussinesq equation," *Journal of Fluid Mechanics,* 49(4), 625–633.

Camfield, F. E., and Street, R. L., (1969). "Shoaling of solitary waves on small slopes," *Journal of Waterway and Harbor Division, ASCE,* 1, 1–22.

Carrier, G. F. and Greenspan, H. P., (1958). "Water waves of finite amplitude on a sloping beach," *Journal of Fluid Mechanics*, 4, 97–109.

Daily, J. W. and Stephan, S. C., (1952). "The solitary wave: its celerity, profile, internal velocities and amplitude attenuation in a horizontal smooth channel," *Proceedings of 3rd Conference of Coastal Engineering,* 13-30.

Enet, F., Grilli, S. T., and Watts, P. (2003). "Laboratory experiments for tsunamis generated by underwater landslides: comparison with numerical modeling," *Proceedings of the 13th Offshore and Polar Engineering Conference*, Honolulu, Hawaii, 3, 372–379.

Falcon, E., Laroche C., and Fauve, S., (2002). "Observation of Depression Solitary Waves on a Thin Fluid Layer," *Phys. Rev. Lett.*, 89, 204501-1.

Fenton, J. D. (1972), "A ninth-order solution for the solitary wave," *J. Fluid Mech.*, Cambridge, England, 53, 257-271.

Goring, D. G., (1979). ''Tsunami: The propagation of long waves onto a shelf," *Report No. KH-R-12-38*, W. M. Keck Laboratory of Hydraulics and Water Resources, California Institute of Technology, Pasadena, California.

Goring, D. G., and F. Raichlen, (1992). "Propagation of long waves onto shelf," *Journal of Waterway, Port, Coastal and Ocean Division,* 118, 43–61.

Grilli, S. T., Losada, M. A. and Martin, F. (1994). "Characteristics of solitary wave breaking induced by breakwaters," *Journal of Waterways, Port, Coastal and Ocean Engineering* 120(1), 74–92.

Grilli, S. T., Svendsen, I. A., and Subramanya, R., (1997). "Breaking criterion and characteristics for solitary waves on slopes," *Journal of Waterway, Port, Coastal, and Ocean Engineering*, 123(3), 102–112.

Grilli, S. T. and Watts, P. (1999) "Modeling of waves generated by a moving submerged body: Applications to underwater landslides," *Engineering Analysis with Boundary Elements*, 23(8), 645–656.

Grilli, S. T. and Watts, P., (2001). "Modeling of tsunami generation by an underwater landslide in a 3-D numerical wave-tank," *Proc. of the 11th Offshore and Polar Engrg. Conf., ISOPE01*, Stavanger, Norway, 3, 132–139.

Grilli, S.T. & Watts, P. (2005), "Tsunami Generation by Submarine Mass Failure. I: Modeling, Experimental Validation, and Sensitivity Analyses," *Journal of Waterway, Port, Coastal, and Ocean Engineering,* 131, 283-297.

Grimshaw, R. (1971), "The solitary wave in water of variable depth. Part 2," *J. Fluid Mech.*, Cambridge, England, 46, 611-622.

Guignard, S., Marcer, R., Rey, V., Kharif, Ch., and Ph. Fraunie, (2001). "Solitary Wave Breaking on Sloping Beaches: 2D two-phase Flow Numerical Simulation by SL-VOF Method," *European Journal of Mechanics, B-Fluids*, 20, 57–74.

Guizien, K. and Barthelemy E. (2002). "Accuracy of Solitary Wave Generation by a Piston Wave Maker", *Journal of Hydraulic Research,* 40(3), 321-331.

Hall, J. V., and Watts, J. W., (1953). "Laboratory investigation of the vertical rise of solitary waves on impermeable slopes.'' *Tech. Memo. 33, Beach Erosion Board*, *U.S. Army Corps of Engineers*.

Hammack, J. L. (1972), "Tsunamis--A Model of Their Generation and propagation". M**.** Keck Laboratory of Hydraulics and Water Resources, Report No. KH-R-28, California Institute of Technology, Pasadena, California.

Hammack, L. J., (1973). "A Note on Tsunamis: Their Generation and Propagation in an Ocean of Uniform Depth," *Journal of Fluid Mechanics,* 60, 769–799.

Hammack, J.L. and Segur, H. (1974). "The Korteweg-de Vries equation and water waves. Part 2. Comparison with experiments", *J. Fluid Mech.,* 65p 289-314.

Hammack, J. L. and Segur, H., (1978). "Modeling criteria for long water waves," *Journal of Fluid Mechanics,* 84, 359–373.

Havelock, T. H., (1929). “Forced surface waves on water,” *Philosophy Magazine,* 8, 569–577.

Heinrich, P., (1992). “Non-Linear Water Waves Generated by Submarine and Aerial Landslide,” *Journal of Waterway, Port, Coastal, and Ocean Engineering*, 118, 249–266.

Hibberd, S. and Peregrine, D. H., (1979). “Surf and Run-up on a Beach: a Uniform Bore,” *Journal of Fluid Mechanics,* 95 (2), 323–345, 1979.

Ho, D. V., Meyer, R. E., (1962). “Climb of a bore on a beach. Part 1: Uniform beach slope.” *Journal of Fluid Mechanics,* 14, 305–318.

Jensen A, Pedersen G. K. and Wood D. J., (2003). “An experimental study of wave run-up at a steep beach,” *Journal of Fluid Mechanics,* 486, 161–188.

Jensen, A., Mayer S., Pedersen G. K., (2005), “Experiments and computation of onshore breaking solitary waves,” *Measurement Science and Technology*, 16, 1913-1920.

Johnson, J. W. and Bermel, K. J., (1949). “Impulsive waves in shallow water as generated by falling weights,” *Transactions of American Geophysical Union,* 30, 223-230.

Kamphuis, J. W. and R. J. Bowering (1972). Impulse waves generated by landslides. In *Proc. of 12th ICCE, ASCE*, pp. 575 - 588.

Kanoglu, U., and Synolakis, C. E., (1998). ‘‘Long wave runup on piecewise linear topographies,’’ *Journal of Fluid Mechanics*, 374, 1– 28.

Kanoglu, U. (2004) “Nonlinear evolution and runup-rundown of long waves over a sloping beach,” *J. Fluid Mech*. 513, 363–372.

Kennard, E. H., (1949). “Generation of surface waves by a moving partition,” *Quarterly Journal of Mechanics and Applied Mathematics,* 7, 303–312.

Keulegan, G. H. (1948). “Gradual damping of solitary waves”, *J. Res. Nat. Bur. Standards*, 40, 487-498.

Kimmoun, O., Branger, H., and Zuchinni, B., (2004). “Laboratory PIV measurements of wave breaking on a beach,” *Proceedings of 14th Offshore and Polar Engineering Conference.*

Kishi, T. and Saeki, H., (1966). “The shoaling, breaking and runup of the solitary wave on impermeable rough slopes impermeable rough slopes,” *Proceedings of 10th Conference on Coastal Engineering*, I, 322–348.

Korteweg, D. J. and de Vries, G., (1895). “On the change of form of long waves advancing in a rectangular canal, and on a new type of long stationary waves,” *Philos. Mag.*, 39**,** 422–443.

Li, Y., (2000). "Tsunamis: non-breaking and breaking solitary wave runup," Report No. KH-R-60, W. M. Keck Laboratory of Hydraulics and Water Resources, California Institute of Technology, Pasadena, California.

Li, Y., Raichlen, F., (2001). "Solitary Wave Runup on Plane Slopes." *Journal of Waterway, Port, Coastal, and Ocean Engineering*, 127(1), 33– 44.

Li, Y., Raichlen, F., (2002). "Non-breaking and breaking solitary wave runup," *Journal of Fluid Mechanics*, 456, 295–318.

Lin, P., Chang, K.-A. and Liu, P. L.-F. (1999). "Runup and run-down of solitary waves on sloping beaches," *Journal of Waterway, Port, Coastal, Ocean Engineering,* 125, 247–255.

Lin, C., Chang, S.-C., Ho, T.-C., Chang, K.-A., (2006). "Laboratory Observation of Solitary Wave Propagating over a Submerged Rectangular Dike," *Journal of Engineering Mechanics*, 132(5), 545–554.

Liu, P. L.-F, Wu, T.-R., Raichlen, F., Synolakis, C. E. Borrero, J. C., (2005). "Runup and rundown generated by three-dimensional sliding masses," *Journal of Fluid Mechanics,* 36, 107–144.

Liu, P. L.-F., Cho, Y., Briggs, M. J., Kanoglu, U., and Synolakis, C. E., (1995). "Runup of solitary waves on a circular island," *Journal of Fluid Mechanics*, 302, 259–285.

Losada, M. A., Vidal, C., Medina, R., (1989). "Experimental study of the evolution of a solitary wave at an abrupt junction," *Journal of Geophysical Research,* 94(C10), 14557–14566.

Madsen, O. S. and Mei, C. C. (1969) "The transformation of a solitary wave over an uneven bottom," *Journal of Fluid Mechanics*, 39, 781–791.

Magoon, O.T., (1966). "Structural damage by tsunamis," *Proceedings, American Society Civil Engineers, Specialty Conference on Coastal Engineering*, Santa Barbara (California), Oct. 1965, 35-68.

Magoon, O.T., (1962). "The tsunami of May 1960 as it affected Northern California," *ASCE Hydraulics Division Conference*, Davis, California 18 pp.

Meyer, R. E., Taylor, A. D., (1972). "Run-up on beaches," In Waves on Beaches and Resulting Sediment Transport (ed. R. E. Meyer), pp. 357–411.

Meyer, R. E., Taylor, A. D., (1972). "Run-up on beaches," In Waves on Beaches and Resulting Sediment Transport (ed. R. E. Meyer), 357–411.

Miller, R.L., (1968), "Experimental determination of run-up of undular and fully developed bores," *J. Geophys. Res.* 73 (14) pp. 4497–4510.

Nagai,T., Hashimoto, N., Shimizu, K., and Kitamura, F. (1996). “Offshore tsunami profiles observed at the coastal wave stations,” *Proceedings of 25th International Conference on Coastal Engineering (ICCE'96)*, 1465-1477.

Pederson, G. and Gjevik, B. (1983) "Run-up of solitary waves." *Journal of Fluid Mechanics*, Vol. 135, 283-209.

Prins, J. E. (1958). Characteristics of waves generated by a local disturbance. *transactions, American Geophysical Union*, 865 - 874.

Ramsden, J. D., (1993). “Tsunamis: Forces on a vertical wall caused by long waves, bores, and surges on a dry bed." *Report No.* KH-R-54, W. M. Keck Laboratory, California Institute of Technology, Pasadena, California.

Rayleigh Lord, (1876). “On waves,” *Phil. Mag.*, 1, p 257-279.

Rabinovich, A. B. and Thomson, R. E. (2007). “The 26 December 2004 Sumatra Tsunami: Analysis of tide gauge data from the World Ocean: Part 1. Indian Ocean and South Africa,” *Pure Appl. Geophys.*, 164(2/3), 261–308.

Russell, J. S. (1845). “Report on waves,” *Proceedings of 14th Meeting British Association for Advanced Science,* 311–390.

Satake, K. (1994), *Mechanism of the* 1992 *Nicaragua Tsunami Earthquake*, *Geophys. Res. Lett.* 21, 2519–2522.

Satake, K. (1995), *Linear and Non-linear Computations of the* 1992 *Nicaragua Earthquake Tsunami*, Pure appl. geophys. 144, 455–470.

Seabra-Santos, F. J., Renouard, D. P., and Temperville, A. M., (1987). “Numerical and experimental study of the transformation of a solitary wave over a shelf or isolated obstacle,” *Journal of Fluid Mechanics*, 176, 117–134.

Shen, M. C., and R. E. Meyer, (1963). “Climb of a bore on a beach: 3. Run-up,” *Journal of Fluid Mechanics*, 16(8), 113– 125.

Shen, M. C., and R. E. Meyer, (1963). “Climb of a bore on a beach: 3. Run-up,” *Journal of Fluid Mechanics*, 16(8), 113– 125.

Slingerland, R.L. and Voight, B. (1979). “Occurrences, properties and predictive models of landslide generated impulse waves. Rockslides and avalanches,” 2:317-397, Ed. Voight, B. *Developments in geotechnical engineering* 14B. Elsevier, Amsterdam.

Sue, L. P., Stokes, R. I., Walters, R. A., (2006). “Experimental Modeling of Tsunami Generated by Underwater Landslides,” *Science of tsunami hazards,* 24(4), 234–265.

Svendsen, I. A. (1974), “Cnoidal waves over a gently Sloping bottom,” Series Paper No. 6, Institute of Hydrodynamics and Hydraulic Engineering, Technical University of Denmark,

Synolakis, C. E., (1986). “The runup of long waves.’’ PhD thesis, California Institute of Technology, Pasadena, California.

Synolakis, C. E., (1987). “The runup of solitary waves.’’ *Journal of Fluid Mechanics*, 185, 523–545.

Synolakis, C. E. (1990). “Generation of long waves in laboratory,” *Journal of Waterway, Port, Coastal, and Ocean Engineering*, 116(2), 252-266.

Synolakis, C. E., Bernard, E.N. (2006). “Tsunami science before and beyond Boxing Day,” *Phil. Trans. R. Soc. A* 364, 2231–2265.

Tadepalli, S. and Synolakis, C. E. (1994) "The run-up of N-waves on sloping beaches." Proceedings of the Royal Society of London: Series *A* – Mathematical Physical and Engineering Science, A, Vol. 445, 99-112.

Tadepalli, S., Synolakis, C. E. (1996) “Model for the leading waves of tsunamis,” *Phys. Rev. Lett.* 77: 2141-2144

Tanaka, M., (1986). “The stability of solitary waves,” *Physics of Fluids,* 29, 650–655.

Teng, M. H., (1997), “Solitary wave solution to Boussinesq equations,” Technical Note, ASCE *J. Waterway, Port, Coastal Ocean Engng,* 123, 138-141.

Tsuji, Y., Namegaya, Y.,Matsumoto, H., Iwasaki, S.-I., Kanbua, W., Sriwichai, M., and Meesuk, V. (2006), The 2004 Indian tsunami in Thailand: Surveyed runup heights and tide gauge records, *Earth Planets Space*, 58, 223–232.

Tuck, E. O., and Hwang, L.-S., (1972). “Long wave generation on a sloping beach,” *Journal of Fluid Mechanics*, 51, 449–461.

Walder, J. S., Watts, P., and Waythomas, C. F., (2006). “Mapping tsunami hazards associated with debris flow into a reservoir,” *Journal of Hydraulic Engineering*, 132(1), 1–11.

Walder, J. S., Watts, P., Sorensen, O. E., and Janssen, K., (2003). “Tsunamis generated by subaerial mass flows,” *J. Geophys. Res.*, 108, 2236–2255.

Watts, P. (1997). “Water waves generated by underwater landslides,” PhD thesis, California Institute of Technology, Pasadena, CA.

Watts, P. (1998). “Wavemaker curves for tsunamis generated by underwater landslides,” *Journal of Waterway, Port, Coastal, and Ocean Engineering*, 124(3), 127–137.

Watts, P., (1997). “Water waves generated by underwater landslides,” PhD thesis, California Institute of Technology, Pasadena, CA.

Watts, P., (2000). “Tsunami Features of Solid Block Underwater Landslides,” *Journal of Waterway, Port, Coastal, and Ocean Engineering*, 126, 144–152.

Whitham, G. B. (1958) “On the propagation of shock waves through regions of non-uniform area of flow.” *J. Fluid Mech.* 4, 337–360.

Wiegel, R. L. (1955). “Laboratory studies of gravity waves generated by the movement of a submerged body,” *Transactions of American Geophysical Union,* 36, (5), 759 - 774.

Wood, D., Pedersen, G. and Jensen, A., (2003). “Modeling of run-up of steep non-breaking waves,” *Ocean Engineering,* 30, 625–644.

Yeh, H. H., Ghazali A. and I. Marton, (1989) “Experimental study of bore run-up,” *J. Fluid Mech.* 206, pp. 563–578.

Yeh, H. H. and Ghazali, A., (1988). “On bore collapse,” *J. Geophys. Res.* 93 (C6), pp. 6930–6936.

Yeh, H., (1991). “Tsunami bore runup,” *Natural Hazards* 4 (2 & 3), 209–220.

Yeh, H., Imamura, F., Synolakis, C. E., Tsuji, Y., Liu, P., and Shi, S., (1993). “The Flores Island Tsunami,” *Transactions of American Geophysical Union,* 74(33), 371–373.

Zelt, J. A. (1991). “The runup of nonbreaking and breaking solitary waves,” *Coastal Engineering*, 15(3), 205–246.

Zelt, J. A., (1986). “Tsunami: The response of harbors with sloping boundaries to long wave excitation,” *Report No. KH-R-47*, W. M. Keck Laboratory of Hydraulics and Water Resources, California Institute of Technology, Pasadena, California.